HHS Public Access

Author manuscript

Immunity. Author manuscript; available in PMC 2024 February 21.

Published in final edited form as:

Immunity. 2023 February 14; 56(2): 386–405.e10. doi:10.1016/j.immuni.2023.01.010.

Tissue-specific abundance of interferon-gamma drives regulatory T cells to restrain DC1-mediated priming of cytotoxic T cells against lung cancer

Maria Zagorulya[1,2], **Leon Yim**[1], **Duncan M. Morgan**[1,3], **Austin Edwards**[4], **Elen Torres-Mejia**[1], **Noor Momin**[1,5], **Chloe V. McCreery**[1,5], **Izabella L. Zamora**[1,6], **Brendan L. Horton**[1], **James G. Fox**[5,7], **K. Dane Wittrup**[1,3,5], **J. Christopher Love**[1,3,8], **Stefani Spranger**[1,2,8,*]

[1]Koch Institute for Integrative Cancer Research, MIT, Cambridge, MA 02139, USA

[2]Department of Biology, MIT, Cambridge, MA 02139, USA

[3]Department of Chemical Engineering, MIT, Cambridge, MA 02139, USA

[4]Biological Imaging Development CoLab, UCSF, San Francisco, CA 94143, USA

[5]Department of Biological Engineering, MIT, Cambridge, MA 02139, USA

[6]Department of Electrical Engineering and Computer Science, MIT, Cambridge, MA 02139, USA

[7]Division of Comparative Medicine, MIT, Cambridge, MA 02139, USA

[8]Ragon Institute of MGH, MIT and Harvard, Cambridge, MA 02139, USA

SUMMARY

Local environmental factors influence $CD8^+$ T cell priming in lymph nodes (LN). Here, we sought to understand how factors unique to the tumor-draining mediastinal LN (mLN) impact $CD8^+$ T cell responses toward lung cancer. Type-1 conventional dendritic cells (DC1) showed a mLN-specific failure to induce robust cytotoxic T cells responses. Using regulatory T (Treg) cell depletion strategies, we found that Treg cells suppressed DC1 in a spatially coordinated manner within tissue-specific microniches within the mLN. Treg cell suppression required MHCII-dependent contact between DC1 and Treg cells. Elevated levels of IFNγ drove differentiation Treg cells into T_H1-like effector Treg cells in the mLN. In patients with cancer, Treg cell T_H1-polarization, but not $CD8^+$/Treg cell ratios, correlated with poor responses to checkpoint blockade

*Corresponding author and lead contact. spranger@mit.edu.

AUTHOR CONTRIBUTIONS

M.Z. and S.S. conceptualized the study. M.Z., B.L.H., E.T.-M. and S.S. designed experiments and interpreted data. M.Z., L.Y., D.M.M. and E.T.-M. performed experiments and analyzed data. A.E., C.V.M. and I.L.Z. conducted spatial analyses. M.Z., D.M.M. and A.E. developed methodology. N.M. and K.D.W. donated resources. J.G.F supervised the study with germ-free mice. M.Z. and S.S. wrote the original draft. M.Z., L.Y., D.M.M., B.L.H., E.T.-M., A.E. and S.S. reviewed and edited the manuscript. S.S. and J.C.L. acquired funding. S.S. supervised the study.

DECLARATION OF INTERESTS

S.S. is a SAB member for Related Sciences, Arcus Biosciences, Ankyra Therapeutics and Venn Therapeutics. S.S. is a co-founder of Danger Bio. S.S. is a consultant for TAKEDA, Merck, Tango Therapeutics, and Ribon Therapeutics and receives funding for unrelated projects from Leap Therapeutics. J.C.L. has interests in Sunflower Therapeutics PBC, Pfizer, Honeycomb Biotechnologies, OneCyte Biotechnologies, SQZ Biotechnologies, Alloy Therapeutics, QuantumCyte, Amgen, and Repligen. S.S. and J.C.L.'s interests are reviewed and managed under MIT's policies for potential conflicts of interest. J.C.L. receives sponsored research support at MIT from Amgen, the Bill & Melinda Gates Foundation, Biogen, Pfizer, Roche, Takeda, and Sanofi.

immunotherapy. Thus, IFNγ in the mLN skew Treg cells to be T_H1-like effector Treg cells, driving their close interaction with DC1 and subsequent suppression of cytotoxic T cell responses.

Keywords

Regulatory T cells; cross-presenting dendritic cells; cytotoxic T cells; T cell dysfunction; T cell priming; anti-tumor immunity; non-small cell lung cancer; interferon-gamma; T_H1-like effector regulatory T cells; tissue-specific immunity

INTRODUCTION

Cytotoxic $CD8^+$ T cells are essential for anti-tumor immunity[1,2]. Naïve $CD8^+$ T cells acquire cytotoxic function following priming by type-1 conventional dendritic cells (DC1) in the tumor-draining lymph nodes (tdLN)[3–5]. DC1 prime naïve T cells by providing three distinct stimulatory signals[6]. Signal 1 is cognate antigen, cross-presented on the major histocompatibility complex class I (MHCI) on DC1[4,5,7,8]. Signal 2 comprises costimulatory ligands, such as CD80 and CD86, expressed on activated DC1[9–13], and signal 3 refers to cytokines, including DC-derived interleukin-12 (IL-12), that promote differentiation into cytotoxic T lymphocytes (CTL)[14–17]. The functional capacity of activated $CD8^+$ T cells depends on the abundance, timing and context of these signals on DC1[18–22].

Distinct T cell activation trajectories established early after priming can have long-term effects on the quality of $CD8^+$ T cell responses. For instance, elevated TOX expression four days post-chronic viral infection mediates commitment to the T cell exhaustion program[23]. In lung cancer, priming induces a T cell dysfunction program that prevents CTL differentiation and drives resistance to immune checkpoint blockade (ICB) therapy[24]. Hence, DC1-derived signals available during priming are instrumental for shaping the quality of the anti-tumor T cell response[25].

The local environment regulates DC capacity to prime T cell responses[25]. At baseline, DC have low expression of signals 2 and 3 and are poorly stimulatory[26–29]. In the absence of signals 2 and 3, cognate antigen-presenting DC induce T cell tolerance, characterized by initial proliferation with failed accumulation and eventual T cell deletion[30–32]. Exposure to danger signals, such as tumor-derived dsDNA, promotes DC maturation and expression of signal 2 and 3 molecules[27–29]. DC stimulatory capacity can be regulated by other immune cells, most notably by regulatory T (Treg) cells. Treg cells inhibit DC maturation and cause decreased expression of signals 2 and 3[33–39]. Treg cell-mediated suppression of DC stimulatory capacity in tumors can blunt protective anti-tumor $CD8^+$ T cell responses[38,40,41]. Additionally, tissue-specific factors and microanatomical niches in the draining LN influence DC ability to prime distinct T cell subsets[42]. For instance, DC in lung and gut LN can imprint tissue-specific homing receptor expression on T cells[43–45]. Moreover, DC can skew T cell responses towards effector, tolerance, or memory programs in a tissue-specific manner[46,47]. Within a draining LN, the microanatomical location of DC1 and $CD8^+$ T cells during priming dictates T cell exposure to stimulatory signals and influences effector differentiation[48,49]. Thus, several environmental factors can impact the T cell activation program induced during priming.

How tissue-specific immunoregulatory mechanisms influence anti-tumor T cell responses remains poorly understood. In this study, we sought to uncover lung cancer-specific mechanisms driving dysfunctional tumor-reactive $CD8^+$ T cells during T cell priming[24]. By comparing T cell responses in the mediastinal (mLN) and inguinal (iLN) LN that drained lung and flank tumors, respectively, we determined that Treg cells in the mLN restrained DC1-mediated priming of CTL more effectively than their counterparts in the iLN. Treg cell-driven suppression of DC1 caused dysfunctional $CD8^+$ T cell responses against lung tumors and required MHCII-dependent contact between Treg cells and DC1. Suppressive, clonally-expanded T_H1-like Treg cells were preferentially induced in the mLN in response to the tissue-specific abundance of interferon-gamma (IFNγ). Blockade of IFNγ was sufficient to repolarize Treg cells and rescue CTL responses against lung tumors. Thus, tissue-specific induction of T_H1-like Treg cells that suppress DC1-mediated CTL priming could represent a critical barrier to anti-tumor immunity.

RESULTS

DC1 in mLN prime dysfunctional $CD8^+$ T cells against lung KP tumors

To study how priming of CTL is restrained in lung cancer[24], we compared T cell responses against tumors growing orthotopically in the lungs or subcutaneously in the flanks. We used the *Kras*^{G12D} *Trp53*$^{-/-}$ (KP) lung adenocarcinoma cell line, engineered to express the model antigen SIIINFEKL fused to ZsGreen (KP-zSIIN)[24,50]. We examined activation of SIIN-reactive $CD8^+$ T cells in the mLN and iLN 7 days post-tumor implantation (Figure 1A). Despite comparable accumulation in both LN, SIIN-reactive T cells primed in the mLN failed to express effector differentiation markers CD25 and Granzyme B (GzmB) (Figure 1B), consistent with prior work[24]. This dysfunctional phenotype contrasted with the robust expression of effector molecules on SIIN-reactive T cells primed in the iLN (Figure 1B). Induction of CTL in the iLN was underscored by the increased expression of TIM3 relative to the mLN (Figure 1C).

We validated that the observed phenotypic and functional differences[24] were independent of TCR signal strength using an *in vivo* priming assay. SIIN-reactive OT-I T cells activated in the mLN exhibited robust proliferation, yet reduced expression of CD25, GzmB, and TIM3 (Figures 1D-F;S1A-B). We affirmed that the dysfunction phenotype was not specific to the SIIN antigen using KP-SIY (SIYRYYGL) cells[24] (Figures S1C-E).

Given the importance of cross-presenting DC1 for mounting anti-tumor immune responses[4,51], we next tested whether DC1 were the dominant DC subset priming tumor-reactive T cells in both LN. SIIN-reactive T cell activation against both lung and flank tumors was severely impaired in *Batf3*$^{-/-}$ mice, lacking DC1[4] (Figures 1G-I;S1F-K). We further validated the requirement of DC1 for priming tumor-reactive T cells in the mLN using the *XCR1*^{DTR} mouse model[52] (Figures 1J-L) and KP-SIY tumor cells (Figures S1L-M). Since DC2 can also prime productive anti-tumor $CD8^+$ T cell responses[53], we compared the functional capacity of DC1 and DC2 for activating $CD8^+$ T cells. Using ZsGreen (ZsG) fluorescence as a readout for tumor antigen uptake, we isolated ZsG^+ and ZsG^- DC1 and DC2 from both tdLN for *ex vivo* co-cultures (Figure S1N). ZsG^+ DC but not ZsG^- DC induced robust T cell proliferation, confirming that tumor-associated antigen was restricted

to the ZsG^+ fraction (Figure S1O-P). While both ZsG^+ DC subsets could activate T cells, only ZsG^+ DC1 induced productive priming, resulting in enhanced T cell proliferation and accumulation (Figure S1O-P). These data indicate that DC1 were the main DC subset activating tumor-reactive $CD8^+$ T cells in both tdLN.

DC1 in tumor-draining mLN have high signal 1, but low signals 2 and 3

DC exist in distinct functional states with varied expression of signals 1 (antigen), 2 (costimulation) and 3 (cytokines), which shape the quality of anti-tumor immunity[53,54]. Since DC1 primed phenotypically distinct $CD8^+$ T cell responses in the tumor-draining mLN and iLN (Figures 1A-L;S1A-M), we hypothesized that tissue-specific differences in DC1 states mediated the distinct priming outcomes. Therefore, we characterized signals 1, 2 and 3 on tumor-derived ZsG^+ DC1 in both tdLN (Figures 2A-B).

ZsG^+ DC1 abundance was increased in the mLN compared to the iLN, with similar ZsG intensity, suggesting no defect in DC1 ability to engulf tumor debris and migrate to the tumor-draining mLN (Figure 2C). ZsG^+ DC1 from both LN also had equal ability to prime naive $CD8^+$ T cells *ex vivo* (Figures S1N-P), underscoring that DC1 from the mLN were not deficient in signal 1. Expression of CD80 and CD86 was reduced, while CD40 was unchanged on ZsG^+ DC1 from mLN compared to those in the iLN (Figure 2D). Further, ZsG^+ DC1 from the mLN produced less IL-12 relative to their counterparts in the iLN (Figure 2E). Since low expression of signals 2 (CD80 and CD86) and 3 (IL-12) is characteristic of immature DC[55,56], we examined the maturation markers MHCII and CCR7. Both molecules were highly expressed on ZsG^+ DC1 from the mLN (Figure 2F). We concluded that tumor-derived DC1 in the mLN were highly mature and provided sufficient signal 1, yet had reduced expression of CD80, CD86 and IL-12, required for priming of true CTL.

Since mature DC can acquire immunoregulatory molecules (mregDC) and suppress anti-tumor immunity following engulfment of tumor debris[54], we examined mregDC markers (CD40, IL-12 and PD-L1)[54]. We observed similar expression of CD40 (Figure 2D) while IL-12 and PD-L1 were reduced on ZsG^+ DC1 from mLN relative to iLN (Figures 2E;S1Q-R). Further, the mLN-specific decrease in CD80, CD86 and IL-12 expression (Figures 2D-E) was also detected on ZsG^- DC1 (Figures S1S-U), suggesting a tissue-specific suppression distinct from the mregDC program.

Reduced expression of CD80, CD86 and IL-12 on DC1 from the tumor-draining mLN (Figures 2D-E;S1S-U) could indicate DC1-intrinsic tissue-specific suppression. However, the tissue-specific differences in signal 2 and 3 on DC1 (Figures 2D-E;S1S-U) were no longer detectable in naïve mice (Figures S1V-X), suggesting that the suppressed phenotype was not an intrinsic property of DC1 in the mLN. Additionally, in contrast to the mLN-specific induction of dysfunctional $CD8^+$ T cells *in vivo* (Figures 1D-E), ZsG^+ DC1 from both LN primed CTL with a similarly high expression of CD25 and GzmB *ex vivo* (Figures S1Y-Z). Thus, the dysfunctional $CD8^+$ T cell responses in the tumor-draining mLN did not result from DC1-intrinsic defects, but instead a DC-extrinsic, mLN-specific and tumor-dependent factor restrained CTL activation *in vivo*.

Treg cells can induce CD8+ T cell dysfunction and DC1 suppression

Treg cells can suppress DC stimulatory capacity by depleting surface molecules CD80 and CD86[34,35,37–39]. Given the low expression of CD80 and CD86 on ZsG+ DC1 from tumor-draining mLN (Figure 2D), we hypothesized that Treg cells inhibited DC1 and thereby caused dysfunctional CD8+ T cell responses in the mLN.

We used *FoxP3*^{DTR} mice[57] to examine the impact of constitutive Treg cell depletion on SIIN-reactive CD8+ T cell responses in the tumor-draining mLN and iLN (Figure 3A). Expression of CD25 and GzmB on tumor-reactive T cells was markedly increased upon Treg cell depletion in both LN (Figure 3B). The rescue of both CD25 and GzmB expression on tumor-reactive T cells was greater in the mLN (Figure 3C), suggesting a more profound Treg cell suppression in the mLN compared to the iLN. While other tissue-specific suppressive factors cannot be fully excluded, these data provided a strong rationale to study the role of Treg cells in shaping the quality of tumor-specific T cell responses in the mLN.

As constitutive Treg cell ablation causes severe autoimmunity[57], we further assessed the impact of transient Treg cell depletion. Transient depletion likewise restored CTL priming in the mLN (Figures 3D-G). Transient Treg cell depletion also led to an increased expression of CD80 and CD86, but not IL-12 on ZsG+ DC1 from the mLN (Figures 3H-J). Similar effects were observed in the iLN (Figures S1AA-AC). Therefore, Treg cells suppressed tumor-reactive T cell responses and DC1 stimulatory capacity in both LN, however, their inhibition of CTL priming was more potent in the mLN.

Treg cells from the tumor-draining mLN restrain cytotoxic T cell priming by suppressing DC-derived signals 2 and 3

As DC1 were required for T cell priming in the mLN (Figure 1) and Treg cells suppressed CTL differentiation (Figure 3), we hypothesized that mLN Treg cells restrained CD8+ T cell priming by inhibiting DC1. To delineate the effects of DC1 and Treg cells on CD8+ T cell priming, we utilized reductionist *ex vivo* co-cultures of naïve OT-I T cells with ZsG+ DC1 and Treg cells isolated from the tumor-draining mLN (Figure 4A; see methods for details). Treg cells caused a stark reduction in CD25 and GzmB expression on OT-I T cells at low Treg:OT-I T cell ratios (Figures 4B-D), while CD8+ T cell proliferation was only mildly reduced (Figures 4D;S2A-B). The resulting CD25^{low} GzmB^{low} phenotype recapitulated the CD8+ T cell dysfunction phenotype observed *in vivo* (Figure 1E). To test whether Treg cells required DC1 to induce dysfunctional CD8+ T cells, we used plate-bound anti-(α)CD3 and αCD28 to stimulate OT-I T cells (Figure 4A). In the absence of DC1, the same number of Treg cells minimally impacted CD25 and GzmB expression on OT-I T cells (Figures 4C-D). Thus, Treg cells could redirect DC1-mediated priming of CTL towards dysfunction yet required the presence of DC1 for this suppression.

To ascertain whether CD8+ T cell states from the *ex vivo* co-cultures (ZsG+ DC1:OT-I ± Treg cells, Figures 4A-D) and the *in vivo* priming assay (mLN versus iLN, Figures 1D-F) were comparable beyond phenotypic markers, we performed single-cell RNA sequencing (scRNA-seq) of *ex vivo*-primed T cells (Figure S2C). We examined the differentially expressed genes (DEG) between CD8+ T cells primed by DC1 in the

presence or absence of Treg cells (Figure S2D; Table S1). Treg cell presence led to reduced expression of transcripts associated with effector function (*GzmB*, *Il2ra, Il12rb1* and *Il12rb2*) and increased expression of transcripts associated with inhibition of effector T cell differentiation (*Sell, Pecam1, Lef1, Tcf7I, S1pr1, S1pr4*) and T cell fate decisions (*Klf2, Klf3*) on $CD8^+$ T cells[24,58–64] (Figure S2D). The transcriptional profiles of T cells primed *ex vivo* in the presence or absence of Treg cells strongly correlated with the published RNA-seq[24] of T cells primed *in vivo* in the KP-tumor-draining mLN or iLN, respectively (Figures S2E-F). This result indicated that transcriptional differences between mLN- and iLN-primed T cells were largely conserved in T cells primed *ex vivo*.

Next, we directly compared the functional suppressive capacity of mLN and iLN Treg cells. Consistent with the *in vivo* Treg cell depletion data (Figure 3A-C), both mLN and iLN Treg cells inhibited CD25 and GzmB expression on primed $CD8^+$ T cells (Figures 4E-G). However, mLN Treg cells induced more potent suppression than iLN Treg cells, regardless of whether ZsG^+ DC1 were isolated from the mLN or iLN (Figures 4E-G;S2G-H). Tissue-specific differences in Treg cell-intrinsic suppressive capacity were only detectable in the DC1:Treg:OT-I T cell co-cultures, as the αCD3/αCD28-based co-cultures revealed comparable suppression (Figures S2I-J).

To compare DC suppression effects of mLN and iLN Treg cells in a controlled setting, we established co-cultures of mature bone marrow-derived-DC (BM-DC) derived from *p40-IRES-eYFP* IL-12 reporter mouse bone marrow and Treg cells sorted from the tumor-draining mLN and iLN (Figures 4H; see methods for details). Consistent with the *in vivo* data (Figures 2D;3I;S1AB), both mLN and iLN Treg cells suppressed CD80 and CD86 expression on BM-DC (Figures 4I-J). However, mLN Treg cells inhibited CD80 and CD86 expression more effectively (Figures 4I-J), mirroring *in vivo* differences in DC1 costimulatory molecule expression in the mLN and iLN (Figure 2D). Treg cells from the iLN induced increased IL-12 suppression compared to Treg cells from the mLN (Figure 4K), in contrast to the *in vivo* observation (Figure 2E). This discrepancy could be explained by a lack of effector T cells in this assay as T cell-derived IFNγ induces IL-12 expression[65].

Insufficiency of DC-derived stimulatory signals can prevent differentiation of CTL[18,19,31]. If Treg cell-mediated inhibition of signals 2 and 3 on DC1 caused dysfunctional priming of $CD8^+$ T cells in the mLN, then providing signals 2 and 3 exogenously should restore CTL priming. Using ZsG^+ DC1:Treg:OT-I T cell co-cultures, we found that singular addition of αCD28 (signal 2) or IL-12 (signal 3) induced a partial increase of GzmB and high expression of CD25, respectively (Figures 4L-M). However, combining αCD28 and IL-12 led to a synergic effect, completely restoring both GzmB and CD25 expression (Figure 4M). We then examined the impact of αCD28 and IL-12 treatment on $CD8^+$ T cell priming in the mLN of lung tumor-bearing mice (Figure 4N). Consistent with *ex vivo* results, we observed that the combination of αCD28 and IL-12 induced robust CD25 and GzmB expression on the tumor-reactive $CD8^+$ T cells (Figure 4O). Thus, Treg cells in the tumor-draining mLN caused dysfunctional priming of $CD8^+$ T cells due to an enhanced ability to suppress DC1 stimulatory signals.

Treg cells suppress CD8$^+$ T cell priming in the mLN via direct interaction with DC1

Treg cells can suppress DC stimulatory molecules in a contact-dependent or independent manner[34,35]. To first evaluate the spatial arrangement of Treg cells and DC1 during CD8$^+$ T cell priming, we performed immunofluorescence (IF) staining of tumor-draining mLN and iLN from *XCR1$^{DTR.Venus}$* mice after adoptive transfer of CD45.1$^+$ OT-I T cells (Figure 5A). We identified XCR1$^+$ DC1, tumor-reactive OT-I T cells and Treg cells using the endogenous Venus signal, CD45.1 and FoxP3 markers, respectively (Figure 5B; see methods for details). We focused our analysis on the OT-I T cell microniches, defined as circular regions centered at OT-I T cell clusters that contain at least one DC1 (Figure 5B; see methods for details), and evaluated Treg:DC1 proximity by measuring the distance from each Treg cell to its closest DC1. The microniche-associated Treg cells and DC1 were closer to each other in the tumor-draining mLN compared to the iLN (Figures 5B-C;S2K). This spatial proximity of Treg cells and DC1 in the mLN was a microniche-specific effect, since outside of microniches the Treg:DC1 distance was increased (Figure 5C). Microniches in the mLN and iLN were similar in size, and the Treg:DC1 ratio within microniches was also not increased in the mLN (Figure 5D). Increased Treg cell suppression in the mLN was likely driven by the physical proximity of Treg cells and DC1 involved in tumor-specific CD8$^+$ T cell activation.

To test whether Treg cell-mediated suppression of DC1 required direct cell:cell contact, we abrogated their MHCII-dependent interactions. Antibody-mediated MHCII blockade in *ex vivo* ZsG$^+$ DC1:Treg:OT-I T cell co-cultures completely reversed the Treg cell suppression phenotype (Figures 5E-F), suggesting that MHCII accessibility on DC1 was critical for the Treg cell-mediated suppression of CD8$^+$ T cell priming. To test the effect of MHCII ablation on DC1 stimulatory capacity *in vivo*, we generated WT:*H2-Ab1$^{-/-}$* mixed bone marrow chimeras (BMCs) and compared the phenotypes of WT and *H2-Ab1$^{-/-}$* ZsG$^+$ DC1 within the tumor-draining mLN (Figures 5G;S2L-M). MHCII deletion resulted in increased expression of CD80, CD86 and IL12 on ZsG$^+$ DC1 *in vivo* (Figures 5H-I), indicating that Treg cell-mediated suppression effects were conferred to DC1 through MHCII-dependent interactions.

We then examined the impact of DC1-specific MHCII deletion on CD8$^+$ T cell priming *in vivo*. We generated WT, *Batf3$^{-/-}$*:WT and *Batf3$^{-/-}$*:*H2-Ab1$^{-/-}$* mixed BMCs to compare the effect of MHCII$^+$ DC1 (in WT and *Batf3$^{-/-}$*:WT BMCs) and MHCII$^-$ DC1 (in *Batf3$^{-/-}$*:*H2-Ab1$^{-/-}$* BMCs) on CD8$^+$ T cell priming (Figures 5J;S2N-O). DC1-specific MHCII deletion in *Batf3$^{-/-}$*:*H2-Ab1$^{-/-}$* BMCs restored the priming of CTL in the mLN compared to control BMCs (Figure 5K). We independently validated this result using *XCR^{DTR}*:WT and *XCR^{DTR}*:*H2-Ab1$^{-/-}$* mixed BMCs (Figures 5L;S2P-Q). Consistently, the DC1-specific MHCII deletion led to effective priming of CTL in the tumor-draining mLN (Figure 5M). Therefore, MHCII-dependent Treg:DC1 interactions caused DC1 suppression and the associated CD8$^+$ T cell dysfunction in the context of lung tumors.

T$_H$1-like Treg cells expand in tumor-draining mLN

It remained unclear what tissue-specific factor(s) caused Treg cells to be more suppressive in the mLN compared to the iLN. Since increased suppression is often associated with a greater

Treg cell abundance[66,67], we enumerated Treg cells in both tdLN. However, Treg cells were equally abundant (Figures 6A-B) and SIIN-reactive $CD8^+$/Treg cell ratios did not correlate with increased suppression observed in the tumor-draining mLN (Figure S3A).

Treg cells are heterogeneous and have distinct tissue-specific functional specializations and TCR repertoires[68], which could influence their suppressive capacity. To characterize their transcriptional states, we performed scRNA-seq paired with TCR-seq on Treg cells sorted from mLN and iLN of tumor-bearing and naïve mice (Figure 6C). We obtained high quality transcriptomes for 16,249 Treg cells (Figure S3B) and recovered TCRβ sequences from 55.4% of cells, TCRα sequences from 23.1% of cells, and paired TCRβ and TCRα sequences from 14.4% of cells (Figures S3C-D). Initial unsupervised analysis identified four clusters of Treg cells, and we focused subsequent analysis on three clusters of activated Treg cells that exhibited reduced expression of markers and gene sets associated with naïve T cells (Figures S3E-I)[69–71]. Among activated Treg cells, we identified four clusters, including Treg cells enriched for transcripts associated with early activation (*Nr4a1*, *Egr1*, *Egr2*, *Myc*, *Dusp*), proliferation (*Mki67*, *Top2a*, *Stmn1*, *Cenpf*, *Birc5*) and two activated Treg cell clusters (activated c1: *Cxcr3*, *Icos*, *Tigit*, *Prdm1*, *Ctla4*; activated c2: *Rorc*, *Ccr6*, *Il10ra*, *Il18r1*, *Tgfbr2*) (Figures 6D-E; Table S2)[72,73]. Activated c1 Treg cells were markedly enriched in both tdLN compared to the naïve LN, suggesting that this transcriptional program was induced in response to tumor (Figure S3J). As Treg cells can suppress in an antigen-specific manner[74,75] and expand clonally in response to tumors[76–78], we evaluated their clonal expansion. Treg cells expanded clonally in both tdLN, but not in either of the naïve LN (Figures 6F-G). The degree of overall clonal expansion was comparable between tumor-draining mLN and iLN and restricted to the activated c1 Treg cell cluster (Figures 6F-G).

To evaluate Treg cell specificity, we analyzed CDR3 sequences within activated c1 Treg cells. Four public TCRβ sequences were recovered independently from Treg cells in multiple mice and shared across mLN and iLN (Table S3). These sequences were often formed by distinct nucleotide rearrangements, demonstrating a convergence in the TCR repertoire (Table S3). These sequences were much more likely to exhibit clonal expansion than other CDR3β sequences (Figure S3K) and were entirely absent from the naïve iLN or mLN (Table S3), despite a comparable degree of sequence recovery (Figures S3C-D). These data suggested that the Treg cells analyzed here were responsive towards tumor-associated antigens present in both tdLN. While these data did not exclude the possibility that TCR repertoire differences could affect Treg cell suppressive capacity, they suggested that features other than the TCR might be dominant in mediating Treg cell suppressive functions.

The phenotype of activated c1 Treg cells correlated with increased functional suppression capacity (Figures S3L-M), which prompted us to interrogate transcriptional differences in activated c1 Treg cells from the mLN and iLN (Figure 6H; Table S4). Activated c1 Treg cells from the mLN differentially expressed transcripts associated with immunosuppression (*Nrp1, Fgl2* and *Nt5e*)[79–81], IFN response and T_H1-polarization (*Ifngr1, Cxcr3*, *Tbx21*, *Cybb and Ptpn11*)[82–84], while their iLN counterparts were enriched for transcripts associated with T cell activation (*Icos* and *Gcnt1*)[85,86] and Treg cell survival and stability

(*Cd2* and *Satb1*)[87,88] (Figure 6H). Additionally, since T_H2-like Treg cells can effectively suppress anti-tumor immunity[89,90], we examined expression of canonical T_H1-, T_H2- and T_H17-polarizing transcription factors (*Tbx21*, *Gata3* and *Rorc*, respectively) on activated c1 Treg cells. Consistently, *Tbx21* expression was increased in the tumor-draining mLN of all analyzed mice, while *Gata3* and *Rorc* were similarly expressed (Figure S3N). Thus, activated c1 Treg cells were T_H1-polarized in the tumor-draining mLN.

Further flow characterization of Treg cells in the two tdLN revealed increased expression of natural Treg cell markers neuropilin 1 (NRP1) and Helios and effector activation markers PD-1 and CTLA-4 on Treg cells from the mLN (Figures 6I-J;S4A-B). Suppressive molecules NRP1, CTLA-4, CD39 and CD73 were differentially expressed on mLN Treg cells, while TGF-b1 and CD25 were highly expressed on iLN Treg cells (Figures 6J;S4A-D), suggesting qualitatively distinct modes of suppression. Ki67 and FoxP3 expression was similar (Figure S4E). Consistent with scRNA-seq results, T_H1-like markers CXCR3 and T-bet were differentially expressed on mLN Treg cells (Figures 6K). Analysis of T-bet, Gata3 and RORγt expression confirmed the T_H1-polarization, as T-bet was most highly expressed on both bulk and $CD44^+$ $CD62L^-$ effector Treg (eTreg) cells in the mLN compared to the iLN (Figures 6L;S4F) and the frequency of T-bet^+ $CXCR3^+$ T_H1-like eTreg cells was increased in the mLN (Figure S4G). Treg cells in the mLN acquired a T_H1-like effector phenotype enriched in a distinct set of suppression molecules.

As Treg cells directly interacted with DC1 in the mLN (Figure 5), we tested whether DC1 regulated the Treg cell response. While Treg cells expressed PD-1 and CTLA-4 similarly in WT and *Batf3*$^{-/-}$ mice, T-bet was decreased and the frequency of T-bet^+ $CXCR3^+$ T_H1-like eTreg cells was reduced in the absence of DC1 (Figure S4H-L). Thus, DC1 were required for the T_H1-polarization of eTreg cells in the mLN.

Since IFN-regulated transcripts and proteins were preferentially expressed on Treg cells from the mLN compared to the iLN (Figures 6H;6K-L;S4F-G), we hypothesized that IFN-sensing induced T_H1-like Treg cells in the mLN. We used WT:*Ifnar1*$^{-/-}$, WT:*Ifngr1*$^{-/-}$ and WT:*Ifngr1*$^{-/-}$*Ifnar1*$^{-/-}$ mixed BMCs[91,92] to compare the phenotypes of WT and IFN receptor-deficient (KO) Treg cells within the tumor-draining mLN (Figures 7A;S5A-B). While Ifnar1 deletion induced a modest reduction in T-bet and had no impact on CXCR3 expression on Treg cells, Ifngr1 deletion caused a severe reduction of both T-bet and CXCR3 expression (Figures 7B;S5C), consistent with published data[82]. Although FoxP3, CD25, PD-1, CTLA-4 and CD73 expression was unaffected by IFN receptor deletion, CD39 was reduced on Ifngr1-deficient Treg cells in the mLN (Figures S5D-E). Expression of T_H1 markers and CD39 on Treg cells was largely dependent on IFNγ-sensing in the tumor-draining mLN.

We then tested whether induction of T_H1-like eTreg cells similarly depended on IFN-sensing in both tdLN. We generated *FoxP3*$^{DTR.eGFP}$:*Ifnar1*$^{-/-}$, *FoxP3*$^{DTR.eGFP}$:*Ifngr1*$^{-/-}$ and *FoxP3*$^{DTR.eGFP}$:*Ifngr1*$^{-/-}$*Ifnar1*$^{-/-}$ mixed BMCs using congenically-labeled hosts and compared phenotypes of donor-derived WT and IFN receptor-deficient (KO) eTreg cells within the tumor-draining mLN and iLN (Figures S5F-G). These BMCs enabled us to exclude host-derived Treg cells and verify that these radio-resistant cells did not confound

our analysis. Consistent with earlier analysis of bulk Treg cells (Figures 7B;S5C), eTreg cell expression of T-bet and CXCR3 in the mLN depended on IFNγ-sensing (Figures S5H-I). Similarly, Ifngr1 but not Ifnar1 ablation blunted T-bet and CXCR3 expression on eTreg cells in the tumor-draining iLN (Figures S5H-I). Although T-bet$^+$ CXCR3$^+$ T_H1-like eTreg cells were preferentially enriched in the WT immune fraction of the mLN relative to the iLN (Figure S5J), as shown before (Figure S4G), their frequency was comparable between mLN and iLN when Ifngr was ablated (Figure S5J). Hence, the T_H1-like eTreg cell program was IFNγ-dependent in both LN, but was predominantly induced in Treg cells of the mLN.

Since induction of T_H1-like eTreg cells relied on IFNγ-sensing, we hypothesized that the mLN-specific enrichment in T_H1-like eTreg cells could result from a tissue-specific difference in IFNγ abundance. Indeed, IFNγ was 3.78-fold more enriched in the tumor-draining mLN compared to the iLN (Figures 7C-D). In contrast, IL-2 abundance was comparable between the two tdLN (Figures S6A-B). Further, IFNγ measurements from naïve LN mirrored those from tdLN, as IFNγ was more abundant in the mLN compared to matched iLN of naïve mice (Figures 7E-F). The mLN-specific enrichment in IFNγ was independent of tumor presence and was determined by the anatomical location of the LN. As lung microbiome-dependent IFN signals can impact lung-specific immunity[93], we tested whether the tissue-specific differences in IFNγ would be maintained in germ-free (GF) mice. Unlike in specific-pathogen free (SPF) mice, the amount of IFNγ in the mLN and matched iLN of naïve GF mice was equalized (Figure 7G). Therefore, observed mLN-specific abundance of IFNγ was caused by the presence of commensal bacteria.

mLN-specific enrichment in IFNγ drives induction of T_H1-like Treg cells and the associated dysfunctional T cell responses against lung cancer

Treg cells in the mLN expressed the chemokine receptor CXCR3 (Figure 6K), which guides intranodal positioning of effector T cells and facilitates interactions with DC[94–96]. To test whether CXCR3 was functionally required for Treg cells to suppress CTL responses against lung tumors, we generated *FoxP3^{DTR}*:WT and *FoxP3^{DTR}*:*Cxcr3$^{-/-}$* mixed BMCs. We treated both groups with DT to compare the suppressive effects of CXCR3-deficient Treg cells (in *FoxP3^{DTR}*:*Cxcr3$^{-/-}$* BMCs) and WT Treg cells (in *FoxP3^{DTR}*:WT BMCs) on CD8$^+$ T cell priming (Figure S6C). Treg cell-specific deletion of CXCR3 has no impact on the CD8$^+$ T cell phenotype in the tumor-draining mLN (Figures S6D-E), suggesting that several redundant chemokine receptor/ligand pathways might promote Treg:DC communication[97–99].

As IFNγ cytokine and IFNγ-dependent T_H1-like Treg cells were enriched in the mLN (Figures 6K-L;7A-F;S5C;S5H-J), we tested whether IFNγ-sensing could regulate Treg cell ability to suppress CTL priming. We generated *FoxP3^{DTR}*:WT and *FoxP3^{DTR}*:*Ifngr1$^{-/-}$* mixed BMCs and treated the mice with DT to evaluate the impact of the Ifngr1-deficient Treg cells (in *FoxP3^{DTR}*:*Ifngr1$^{-/-}$* BMCs) or WT Treg cells (in *FoxP3^{DTR}*:WT BMCs) on CD8$^+$ T cell priming in the tumor-draining mLN (Figures S6F-G). Compared to the control, Ifngr1 ablation on Treg cells led to increased CD25 expression on CD8$^+$ T cells primed in the mLN (Figures 7H-I). This 2.24-fold increase (±0.374 SEM) (Figures 7H-I) was comparable to the 3.32-fold difference in CD25 expression (±0.947 SEM) between

iLN and mLN-primed T cells (Figure 1E). Although GzmB and TIM3/TCF1 expression was unchanged (Figures 7I;S6H), the partial rescue was encouraging, as roughly half of all immune cells in *FoxP3*^{DTR}:*Ifngr1*$^{-/-}$ BMCs were Ifngr1-deficient, including DC1, which depend on IFNγ for IL-12 production[54,65]. In the absence of DT treatment, CD8$^+$ T cells primed in the mLN of *FoxP3*^{DTR}:WT and *FoxP3*^{DTR}:*Ifngr1*$^{-/-}$ BMCs exhibited unchanged CD25 expression (Figures S6I-K), indicating that the observed rescue effect (Figure 7I) was driven by Treg cell-specific ablation of IFNγ-sensing.

We then evaluated whether antibody-mediated IFNγ blockade could counter the IFNγ-rich environment of the mLN and rewire Treg cell polarization and CD8$^+$ T cell priming. Since IFNγ plays an important role in CD8$^+$ T cell effector differentiation[100–102], we administered IFNγ blockade early post-tumor implantation and evaluated priming of adoptively-transferred T cells (Figure 7J). IFNγ blockade caused increased CD25, GzmB and TIM-3 expression on the OT-I T cells in the tumor-draining mLN (Figure 7K), but had no impact in the tumor-draining iLN (Figures S7A-B), underscoring that this immunoregulation was tissue-specific. Additionally, IFNγ blockade caused decreased T-bet expression in both mLN and iLN Treg cells, while leaving the total number of Treg cells unchanged (Figures 7L;S7C). Transient IFNγ blockade was sufficient to rescue CTL priming and alter the Treg cell phenotype in the IFNγ-rich environment of the tumor-draining mLN.

To examine whether the IFN-dependent T_H1-like Treg cells correlated with blunted anti-tumor immunity in humans, we reanalyzed a scRNA-seq dataset of tumor-infiltrating T cells from human melanoma[103]. Treg cell expression of the IFN response program and either *TBX21* or *CXCR3* transcripts strongly correlated with ICB resistance in these patients (Figures 7M;S7D). The CD8$^+$/Treg cell ratio did not associate with ICB response (Figure 7M), suggesting that the Treg cell quality, rather than quantity, determined anti-tumor immunity outcomes. Combined with our published finding that lung cancer-specific CD8$^+$ T cell dysfunction drives ICB resistance[24], these data suggested that IFNγ-dependent T_H1-like Treg cells correlated with ICB resistance in humans and mice.

DISCUSSION

We established that T_H1-like eTreg cells in the lung tumor-draining mLN restrained activation of anti-tumor CTL and induced a dysfunctional CD8$^+$ T cell state. Mechanistically, Treg cells in the tumor-draining mLN suppressed DC1 stimulatory signals needed to drive successful CTL differentiation. The suppression was mediated via MHCII-dependent contact between Treg cells and DC1 and was associated with the mLN-specific T_H1-like eTreg cell program characterized by increased T-bet and CXCR3 expression. T_H1-like eTreg cells were induced by IFNγ, which was preferentially enriched in the tumor-draining mLN. Antibody-mediated IFNγ blockade could counter the naturally increased IFNγ abundance in the mLN, resulting in Treg cell repolarization and enhanced CTL responses against lung tumors. Additionally, IFNγ-induced T_H1-like Treg cells correlated with ICB resistance in patients with cancer. Collectively, our data suggested that T_H1-like eTreg cells acted on DC1 in the tdLN to prevent priming of CTL responses against lung tumors.

Mounting evidence suggests that the tissue site of tumor growth can influence anti-tumor immunity[104,105]. By directly comparing T cell responses mounted against KP tumor cells implanted into the lungs or flanks of mice, we identified a Treg cell-driven lung-specific mechanism of immunosuppression. Lung tumor growth led to IFNγ-dependent T_H1-like eTreg responses associated with highly potent suppression capacity and enhanced spatial proximity to DC1. These findings are consistent with prior reports describing the importance of IFNγ-sensing T_H1-like Treg cells for suppressing autoimmunity in type-1-diabetes and graft-versus-host disease[106–108]. In addition to restraining CTL priming locally in the lung tdLN, we predict that this Treg cell state could systemically suppress anti-tumor immunity and potentially blunt secondary tumor control, as shown in prior studies[109].

We found that T_H1-like eTreg cell responses in the lung setting were driven by the mLN-specific abundance in IFNγ, which was induced by commensal bacteria. Consistent with our findings, the lung microbiome can directly impact lung-specific immunoregulatory mechanisms[110] as well as anti-tumor immunity[111]. The microbiome has further been reported to regulate the suppression capacity and frequency of Treg cells[112,113]. Local immune populations that respond to commensal bacteria[114], such as unconventional T cells, have been described to migrate to the draining LN and shape conventional T cell responses in a tissue-specific manner[115]. It remains to be determined which cells mediate the mLN-specific abundance in IFNγ observed in this study.

Our observations do not exclude the possibility that Treg cell-independent tissue-specific factors might also contribute to the immunosuppressive microenvironment of the tumor-draining mLN. For instance, tumors from different anatomic sites differ in local nutrient availability[116], and the local metabolic environment directly regulates DC and T cell functions in cancer[117–121]. It is plausible that differential nutrient availability in the tumor-draining iLN and mLN could further promote the qualitatively distinct T cell responses observed in our study.

Establishment of protective anti-tumor immunity requires a breach of immune tolerance[122], however, the mechanisms that maintain peripheral tolerance in cancer remain poorly understood. We uncovered a mechanism of MHCII-dependent Treg cell-mediated DC1 suppression that restrained the activation of a protective anti-tumor T cell response in the tdLN. T_H1-like eTreg cells were the critical mediators of this $CD8^+$ T cell tolerance. Although we described this mechanism in the context of lung tumors, MHCII ablation on DC1 can similarly disrupt peripheral tolerance of $CD8^+$ T cells specific to a keratinocyte-derived self-antigen in the skin[123]. Thus, this peripheral tolerance mechanism is likely generalizable and not restricted to the lung setting. The preferential induction of peripheral tolerance in response to KP lung tumors but not flank tumors suggested that distinct tissue sites might have different tolerance setpoints. Since differential IFNγ abundance regulated Treg cell phenotypes and suppression capacity, tissue-specific availability of cytokines might influence the tolerance setpoint in different contexts. Further research is needed to discern additional stimuli that regulate peripheral tolerance at different anatomic sites. An improved mechanistic understanding of peripheral tolerance regulation could inspire new therapeutic approaches to disrupt immune tolerance against cancer and boost protective anti-tumor immunity.

LIMITATIONS OF STUDY

Our results strongly support the conclusion that IFNγ-sensing by Treg cells leads to enhanced suppression in the mLN. Refined studies utilizing mouse models that harbor Treg cell-specific *Ifngr1*$^{-/-}$ are needed to fully elucidate the molecular mediators of this suppression. Additionally, it is important to further validate this immunoregulatory mechanism in the context of human biology using immune cell co-cultures and spatial analyses of Treg cells, DC1 and CD8^{+} T cells in tdLN of patients.

RESOURCE AVAILABILITY

Lead contact

Further information and requests for resources and reagents should be directed to and will be fulfilled by the lead contact, Stefani Spranger (spranger@mit.edu).

Materials availability

This study did not generate new unique reagents.

Data and code availability

The scRNA-seq data generated in this study has been deposited to the GEO database (GSE216086), and code used to process and analyze scRNA-seq data was made available at https://github.com/duncanmorgan/kptumors_immunity and is archived at https://doi.org/10.5281/zenodo.7331914. Code used for the spatial analysis of IF images was made available at https://github.com/awedwards/DC-Treg-CD8T-interactions-project. Any additional information required to reanalyze the data reported in this paper is available from the lead contact upon request.

EXPERIMENTAL MODEL AND SUBJECT DETAILS

Mice

C57BL/6 mice were purchased from Taconic Biosciences or Jackson Laboratories. *H2-Ab1*$^{-/-}$ mice were purchased from Taconic Biosciences. *Batf3*$^{-/-}$, *FoxP3*$^{DTR.eGFP}$, *p40-IRES-eYFP, Ifnar1*$^{-/-}$, *Ifngr1*$^{-/-}$, *Ifngr1*$^{-/-}$ *Ifnar1*$^{-/-}$, *Cxcr3*$^{-/-}$, *Thy1.1*$^{+}$ and *CD45.1*$^{+}$ mice were purchased from Jackson Laboratories and bred in-house. TCR-transgenic OT-I *Rag2*$^{-/-}$ and *XCR1*$^{DTR.Venus}$ mice were bred and maintained in-house. All mice were housed under specific pathogen free conditions at the Koch Institute animal facility. Mice were gender-matched and age-matched to be 6–12 weeks old at the time of experimentation. All experimental animal procedures were approved by the Committee on Animal Care at MIT.

Cell lines and tumor injections

KP-zSIIN and KP-SIY were cultured at 37°C and 5% CO_2 in DMEM (GIBCO) supplemented with 10% FBS (Atlanta Biologicals), 1% penicillin/streptomycin (GIBCO), and 1X non-essential amino acids (GIBCO). For tumor implantation, tumor cells were harvested by trypsinization (GIBCO), washed twice with 1X PBS (GIBCO), resuspended in PBS and 2.5x10^{5} tumor cells were injected subcutaneously or intravenously.

METHOD DETAILS

Generation of expression vectors and modified tumor cell lines

The pLV-EF1α-IRES-puro vector (Addgene no. 85132) was linearized by digestion with BamHI and EcoRI restriction enzymes (NEB). The ZsGreen-SIINFEKL insert was generated using the pCAGGS_ZsGreen_minOVA construct (a gift from Max Krummel at UCSF), then cloned into the linearized pLV-EF1α-IRES-puro vector using the In-Fusion cloning kit (Takara Bio). The resulting pLV-EF1α-ZsGreen-SIINFEKL-IRES-puro construct was amplified and sequenced for accuracy. The KP-zSIIN cell line was genetically engineered to stably express ZsGreen-SIINFEKL using lentiviral transduction of the KP parental tumor line (a gift from Tyler Jacks) with the pLV-EF1a-cerulean-SIIN-SIY-IRES-puro construct. KP-zSIIN cell line was puromycin (GIBCO) selected and further FACS-sorted to enrich for cells with maximal expression of ZsGreen. Generation of the KP-SIY cell line was previously described[24].

Adoptive transfer of T cells

The *in vivo* priming assay was adapted from Horton *et al.*[24]. Briefly, OT-I T cells were isolated from spleens and LN of *OT-I Rag2*$^{-/-}$ *CD45.1*$^{+}$ mice, labeled with CTV dye (Invitrogen) following manufacturer's instructions and at least 10^6 (for flow analysis) or precisely $2.5x10^4$ cells (for immunostaining) were transferred retro-orbitally (*r.o.*) to mice with KP-zSIIN tumors at day 7 post-tumor implantation. Transferred OT-I T cells were analyzed in tdLN of recipient mice 3 days later. Frequency of proliferated T cells was quantified as the percentage of cells that had undergone one or more rounds of division, gated using an unstimulated, CTV-labeled sample as the undivided reference control. The T cell proliferation index was quantified as the total number of divisions divided by the number of cells that went into division using the proliferation modeling function in FlowJo v10.5.3 software (TreeStar).

Tissue processing for flow cytometry, cell sorting and ELISpot

LN were either directly mashed through a 70 μm filter into RPMI (GIBCO) for T cell analysis, or processed using a method adapted from Ruhland *et al.*[124] for DC analysis and sorting. For the latter, LN were pierced with sharp forceps, incubated for 15 min at 37°C in digestion buffer (250 μg/ml Liberase (Sigma-Aldrich) and 50 μg/ml DNase (Sigma-Aldrich) in RPMI (GIBCO)), then pipetted up and down vigorously, followed by a second 15 min incubation at 37°C. The LN cell mixture was filtered through a 70 μm filter to generate a single cell suspension. For sorting, LN cells were next incubated with αCD16/CD32 (clone 93, BioLegend) in FACS buffer (PBS (GIBCO) with 1% FBS (Atlanta Biologicals) and 2 mM EDTA (Invitrogen)) for 15 min at 4°C to prevent non-specific antibody binding, then washed with FACS buffer. The cells were then incubated with PE-labeled antibodies (αCD19-PE clone 1D3 and αCD3e-PE clone 17A2 if only DC were sorted, or αCD19-PE alone if Treg cells were also sorted, Biolegend) in FACS buffer for 10 min at 4°C, followed by negative selection using anti-PE microbeads (Miltenyi Biotec) according to manufacturer's instructions, prior to staining for FACS. Lungs and flank tumors were dissected, minced, then incubated in digestion buffer for 40 min at 37°C and mashed through a 70 μm filter to generate a single cell suspension. Spleens were dissected and

directly mashed through a 70 μm filter to generate a single cell suspension. ACK Lysing Buffer (GIBCO) was used to lyse red blood cells in lungs and spleens (lysis performed for 2 min on ice, followed by two washes with PBS), prior to staining for flow or plating for ELISpot.

Flow cytometry and FACS staining

Cells were resuspended in FACS buffer (PBS (GIBCO) with 1% FBS (Atlanta Biologicals) and 2 mM EDTA (Invitrogen)) containing Fixable Viability Dye eFluor 780, eFluor 506 or eFluor 405 (eBioscience) to distinguish live and dead cells and αCD16/CD32 (clone 93, BioLegend) to prevent non-specific antibody binding, and incubated for 15 min at 4°C. Cells were then washed with FACS buffer and stained for surface proteins using fluorophore-conjugated antibodies resuspended in FACS buffer at the specified dilutions (Table S5) for 20 min at 4°C. Following surface staining, cells were washed twice with FACS buffer and analyzed directly or fixed for downstream intracellular staining and/or analysis the next day. Cell fixation was achieved using the Foxp3 Transcription Factor Fixation/Permeabilization buffer (eBioscience) when staining for transcription factors, or the Cytofix/Cytoperm Fixation/Permeabilization buffer (BD Biosciences) when staining for cytokines, following manufacturer's instructions. Brefeldin A (BioLegend) was added to all buffers prior to fixation when staining for cytokines. After fixation, cells were washed twice with FACS buffer, stained for intracellular proteins (antibodies and dilutions specified in Table S5) in FACS buffer overnight at 4°C and then washed twice with FACS buffer prior to flow analysis. To obtain absolute counts of cells, Precision Count Beads (BioLegend) were added to samples following manufacturer's instructions. Flow cytometry sample acquisition was performed on a LSR Fortessa cytometer (BD), and the collected data was analyzed using FlowJo v10.5.3 software (TreeStar). For cell sorting, the surface staining was performed as described above under sterile conditions, and cells were acquired and sorted into co-culture media (RPMI (GIBCO) containing 10% FBS (Atlanta Biologicals), 1% penicillin/streptomycin (GIBCO), 1X non-essential amino acids (GIBCO) and 1X β-mercaptoethanol (GIBCO)) using a FACSAria III sorter (BD). For $CD8^+$ T cell analysis, cells were pre-gated on live, singlets, $CD45^+$, $CD3e^+$, $CD4^-$, $CD8^+$ (and $CD45.1^+$ if congenically labeled) markers. For DC analysis and cell sorting, cells were pre-gated on live, singlets, $CD45^+$, $CD19^-$, $CD3e^-$, $NK1.1^-$, $Ly6C^-$, $MHCII^+$, $F4/80^-$, $CD11c^+$ and ZsG^+ if appropriate (also $autofluorescence^-$ in lungs to exclude autofluorescent $CD11c^+$ alveolar macrophages). For Treg cell analysis, cells were pre-gated on live, singlets, $CD45^+$, $CD3e^+$, $CD8^-$, $CD4^+$ and $FoxP3^+$ markers (and eTreg cells were further defined as $CD44^+$ $CD62L^-$ Treg cells). For cell sorting, Treg cells were gated as live, singlets, $CD45^+$, $CD3e^+$, $CD8^-$, $CD4^+$ and $CD25^{high}$ and an example gating strategy is shown in Extended Data S1A.

SIIN-tetramer staining

To identify SIIN-reactive $CD8^+$ T cells, PE-conjugated SIIN tetramer was added during the surface staining step in the flow cytometry methods described above. PE-conjugated SIIN tetramer was assembled in-house using biotinylated peptide-MHC monomer (NIH Tetramer Core Facility) and PE-streptavidin (Invitrogen) following the NIH tetramerization protocol, and titrated to empirically determine the optimal staining concentration.

In vivo mouse treatments

For DT-mediated cell depletion, DT (Sigma-Aldrich) was diluted in PBS (GIBCO) and administered intraperitoneally (*i.p.*) to deplete FoxP3$^+$ Treg cells in *FoxP3*^{DTR} mice, *FoxP3*^{DTR}/WT and *FoxP3*^{DTR}/*Ifngr1*$^{-/-}$ BMCs (1μg DT/mouse) or XCR1$^+$ DC1 in *XCR1*^{DTR} mice, *XCR1*^{DTR}/WT and *XCR1*^{DTR}/*H2-Ab1*$^{-/-}$ BMCs (0.5μg DT/mouse) at the indicated timepoints. For *in vivo* treatments, mice were injected with 100 μg αCD28 antibody *i.p.* (clone 37.51, Bio X Cell), 1.42x10^{-11} mol IL-12 protein fused to murine serum albumin *r.o.* (IL-12-MSA, manufactured in-house) or 200 μg IFNγ antibody *i.p.* (clone XMG1.2, Bio X Cell) at the indicated timepoints.

IFNγ ELISpot

ELISpot plates (EMD Millipore) were coated overnight at 4°C with αIFNγ capture antibody (BD Biosciences). Plates were washed and blocked with complete media (DMEM (GIBCO) supplemented with 10% FBS (Atlanta Biologicals), 1% penicillin/streptomycin (GIBCO), and 1X non-essential amino acids (GIBCO)) for 2 hr at room temperature (RT). Splenocytes were plated in complete media at 10^6 cells/well in the presence or absence of 160 nM SIINFEKL peptide (Invivogen). As a positive control, splenocytes were plated in complete media containing 100 ng/ml PMA (Sigma-Aldrich) and 1 μg/ml ionomycin (Sigma-Aldrich). Plates were incubated overnight at 37°C and 5% CO_2, then developed using the mouse IFNγ ELISpot kit (BD Biosciences), following manufacturer's protocol.

Treg cell transcription factor analysis

To accurately compare differences in Treg cell transcription factor expression, lung and flank KP-zSIIN tumors were implanted into Thy1.2$^+$ and Thy1.1$^+$ mice, respectively, and tdLN from congenically-labeled mice were combined for downstream processing and flow analysis. Relative expression of transcription factor expression were quantified as the ratio of gMFI values for matched Thy1.2$^+$ mLN-derived and Thy1.1$^+$ iLN-derived fractions of bulk or eTreg cells, as indicated. The experiment was repeated with reversed congenic marker assignments, i.e. using tdLN samples from Thy1.1$^+$ lung- and Thy1.2$^+$ flank-tumor-bearing mice, to ensure reproducibility, and the data were pooled. The same experimental approach was used to evaluate transcription factor expression in Treg cells from WT and *Batf3*$^{-/-}$ lung tumor-bearing mice.

Generation of BMC mice

Host mice were irradiated with 500 rad, allowed to recover for 3 hr, and subsequently irradiated again with 550 rad. The next day, BM was harvested from the femur and tibia of donor mice, depleted of T cells using CD90.2 microbeads (Miltenyi Biotec), washed twice with PBS and 10^7 cells were injected *r.o.* into the irradiated host mice. For mixed BM chimeras, 10^7 total cells of a 50:50 mixture of BM from donor mice was transferred. A period of at least 6 weeks was allowed for engraftment prior to the start of experiments.

Ex vivo T cell priming co-cultures

DC and Treg cells were FACS-sorted from LN as described above (LN from many mice were pooled to reach appropriate cell yield). SIIN-reactive CD8$^+$ T cells were isolated

from spleens and LN of naïve OT-I TCR-transgenic mice using the untouched $CD8^+$ T cell isolation kit (Miltenyi Biotec), following manufacturer's instructions. Isolated $CD8^+$ OT-I T cells were washed twice with PBS and stained with CTV dye (Life Technologies) following manufacturer's instructions. For DC:OT-I co-cultures, $5x10^3$ sorted ZsG^+ or ZsG^- DC were cultured with $5x10^4$ dye-labeled $CD8^+$ OT-I T cells, respectively (1:10 DC:T cell ratio). For ZsG^+ DC1:Treg:OT-I T cell suppression co-cultures, $5x10^3$ sorted ZsG^+ DC1 were cultured with $5x10^4$ dye-labeled $CD8^+$ OT-I T cells, in the presence or absence of $6.25x10^3$ sorted Treg cells (1:8 Treg:OT-I ratio), unless indicated otherwise. For Treg:OT-I suppression co-cultures performed without DC1, various numbers of Treg cells were cultured with $5x10^4$ dye-labeled $CD8^+$ OT-I T cells (at the indicated Treg:OT-I ratios) on αCD3/αCD28-coated plates. Antibody-coated plates were coated overnight at 4°C with 0.2 μg/ml αCD3 (clone 145–2C11, BD Biosciences) and 0.5 μg/ml αCD28 (clone 37.51, BD Biosciences) in PBS, washed with PBS, then blocked with co-culture media (RPMI (GIBCO) containing 10% FBS (Atlanta Biologicals), 1% penicillin/streptomycin (GIBCO) and 1X β-mercaptoethanol (GIBCO)) for at least 30 min at RT, prior to adding cells. For all *ex vivo* T cell priming co-cultures, cells were resuspended in co-culture medium, added to V-bottom tissue culture-treated 96-well plates and cultured at 37°C and 5% CO_2 for 3 days. Following co-culture, cells were stained and analyzed by flow cytometry. Frequency of proliferated T cells was quantified as the percentage of cells that had undergone one or more rounds of division, gated using an unstimulated, CTV-labeled sample as the undivided reference control. The T cell proliferation index was quantified as the total number of divisions divided by the the number of cells that went into division using the proliferation modeling function in FlowJo v10.5.3 software (TreeStar). Expression of T cell activation markers was also assessed by flow staining as described. For co-culture experiments performed in the presence of additional biomolecules, 5 μg/ml αCD28 (clone 37.51, BD Biosciences), 10 nM IL-12 (using IL-12-MSA fusion protein generated in-house) or 10 μg/ml αMHCII (clone M5/114, Bio X Cell) were added at the beginning of co-culture where indicated.

Generation of BM-DC

BM-DC generation protocol was adapted from de Mingo Pulido *et al.*[125]. BM was harvested from the femur and tibia of *p40-IRES-eYFP* mice, passed through a 70 μm filter, ACK-lysed and cultured at a density of $2x10^6$ cells/ml in RPMI (GIBCO) supplemented with 10% FBS (Atlanta Biologicals), 1% penicillin/streptomycin (GIBCO), 25 mM HEPES (GIBCO), 1X non-essential amino acids (GIBCO), 10 mM sodium pyruvate (GIBCO), 1X β-mercaptoethanol (GIBCO), 100 ng/ml recombinant human FLT3-L (Bio X Cell), and 5 ng/ml recombinant mouse GM-CSF (BioLegend) for 6 days at 37°C and 5% CO_2. On day 6, floating and semi-adherent cells were collected as BM-DC, frozen in 10% DMSO (Sigma-Aldrich) in FBS (Atlanta Biologicals) and stored in liquid nitrogen.

BM-DC:Treg cell co-cultures

Treg cells were FACS-sorted from LN as described above. Frozen *p40-IRES-eYFP* BM-DC were thawed and cultured in RPMI (GIBCO) supplemented with 10% FBS (Atlanta Biologicals), 1% penicillin/streptomycin (GIBCO), 25 mM HEPES (GIBCO), 1X non-essential amino acids (GIBCO), 10 mM sodium pyruvate (GIBCO), 1X β-mercaptoethanol (GIBCO), 100 ng/ml recombinant human FLT3-L (Bio X Cell), and 5 ng/ml recombinant

mouse GM-CSF (BioLegend) for 2 days at 37°C and 5% CO_2. BM-DC were then washed in PBS and cultured overnight in 1 μg/ml Poly(I:C) (Invivogen) in co-culture media (RPMI (GIBCO) containing 10% FBS (Atlanta Biologicals), 1% penicillin/streptomycin (GIBCO) and 1X β-mercaptoethanol (GIBCO)) at 37°C and 5% CO_2 to generate mature BM-DC. On the next day mature BM-DC were collected and washed twice with PBS, prior to addition to assays. For BM-DC:Treg cell co-cultures, $2x10^4$ mature BM-DC and $2.5x10^4$ sorted Treg cells were resuspended in co-culture medium with 10 nM IL-2 (using IL-2-MSA fusion protein generated in-house), added to V-bottom tissue culture-treated 96-well plates and cultured at 37°C and 5% CO_2 for 24 hr. Following co-culture, cells were stained and analyzed by flow cytometry. A representative gating strategy of BM-DC1 is shown in Extended Data S1B.

Tissue section preparation and immunostaining

Adapted from Gerner *et al.*[126]. LN were harvested, fixed in periodate-lysine-paraformaldehyde buffer (0.05 M phosphate buffer containing 0.1 M lysine, 2 mg/ml NaIO4, and 1% of paraformaldehyde (Electron Microscopy Grade), pH 7.4) overnight at 4°C, followed by cryoprotection in 30% sucrose in PBS for 24 hr at 4°C. LN were then carefully cleaned of fat, embedded in 100% OCT in cryomolds, snap-frozen by floating the cryomolds on a solution of 2-methylbutane cooled by dry ice and stored at −80°C until processing. Frozen LN were completely sectioned (10 μm thickness) using Cryostar NX70 (Thermo Scientific) to make sure that imaged tissue cross-sections contained all representative LN regions. Tissue sections were left to dry for 30 min at RT, post-fixed in ice-cold acetone for 10 min at −20°C, then left to dry again for 30 min at RT and stored at −20°C. For immunostaining, sections were first warmed to RT, washed twice with PBS and incubated with blocking buffer (PBS containing 1% bovine serum albumin, 1% normal mouse serum, 10% normal goat serum, and 0.3% Triton X-100) for 2 hr at RT. Tissue sections were then stained with primary antibody (chicken polyclonal αGFP, 1:1000; abcam) diluted in blocking buffer for 2 hr at RT, washed three times with wash buffer (PBS with 0.3% Triton X-100), followed by staining with secondary antibody (goat anti-chicken AF488 1:500, Jackson ImmunoResearch) diluted in blocking buffer for 1 hr at RT. Next, samples were washed three times with wash buffer and stained with fluorophore-conjugated antibodies (FoxP3-AF750 clone 1054C, 1:100, R&D Systems; CD45.1-APC clone A20, 1:100, Biolegend) diluted in blocking buffer for 1 hr at RT. Then, nuclei were counterstained with 1.5 μm propidium iodide (1:1000, Sigma-Aldrich) diluted in wash buffer for 10 min at RT, followed by a wash in PBS. Samples were mounted using ProLong Diamond Antifade Mountant (Thermo Fisher Scientific).

Imaging

Tissue sections were imaged using the TissueFAXS Plus automated slide scanning system (TissueGnostics, USA) combining a Zeiss Axio Imager 2 upright microscope with a Märzhäuser motorized stage (Märzhäuser Wetzlar). We utilized the Zeiss 20x Plan-Neofluor 0.5 N.A. air objective, in combination with filters sets (from Chroma Technology, USA) with the following specifications: AF488 (470/24) ET470/30x T495lpxr ET515/30m, AF750 (740/20) ET740/40x T770lpxr ET780lp, multiband dichroic qTexasRed/qCy5 (550/15, 640/30). A Lumencor Spectra 3 LED light engine (500 mW per channel) provided

excitation. Fluorescence images were captured using a Hamamatsu Orca Flash 4.0 V2 cooled digital CMOS camera C11440–22CU. Exposure times were 94 ms for AF488, 146 ms for AF750, 10 ms for qTexasRed and 48 ms for qCy5 channels. Tissue sections were acquired as z-stacks in a process called extended focus, with a 3 μm step size, including one step above and one step below the focal plane. Extended focus takes each in-focus area of each image within the z-stack and combines those regions into a single image. Image processing included stitching performed using the TissueFAXS capture/control software.

Image processing and spatial analysis

Images were exported as single channel TIFF files using the TissueFAXS Viewer software (TissueGnostics USA) and downstream image analysis was completed in Imaris software v9.7.2 (Bitplane) and using custom scripts in Python. Imaris Surface objects were created for FoxP3$^+$ Treg cells (smoothing sigma = 0.5μm, intensity threshold = 17.2, seed point diameter = 3.00μm, seed point quality filter = 1.0), XCR1$^+$ DC1 (smoothing sigma = 0.20μm, background subtraction rolling ball radius = 5.00μm, background subtraction threshold = 8.69, seed point diameter = 5.00μm, seed point quality threshold = 2.07, size threshold >= 50.0 voxels), CD45.1$^+$ CD8$^+$ OT-I T cells (smoothing sigma = 0.5μm, intensity threshold = 16.7, seed point diameter = 6.00μm, seed point quality threshold = 4.87, area threshold >= 11.5μm^2) and CD45.1$^+$ CD8$^+$ OT-I T cell clusters (smoothing sigma = 0.5μm, intensity threshold = 9.12, area threshold > 300μm^2). Surfaces for FoxP3$^+$ Treg cells, XCR1$^+$ DC1 cells and CD45.1$^+$ CD8$^+$ OT-I T cells were further segmented using the “Split touching objects” function. A surface was also made for the entire lymph node using the nuclear channel (smoothing sigma = 5.00μm, intensity threshold = 10.0). For each surface set, the surface area and centroid coordinates were exported and collated across images. For each CD8$^+$ OT-I T cell cluster surface, the area of the cluster was used to calculate the radius. The microniche area for each CD8$^+$ OT-I T cell cluster was defined using the radius of the CD8$^+$ OT-I T cell cluster plus 5μm, 10μm, 15μm and 20μm. Distance matrices encoding the distance between the centroid of the CD8$^+$ OT-I T cell cluster and centroids all DC1 and Treg cells in the image were generated. These distance matrices were thresholded using the microniche radius to find the DC1 and Treg cells that were positioned within each microniche. Finally, a new distance matrix was calculated between the DC1 and Treg cells within each microniche to find the minimum distance from each Treg cell to a DC1. Code made available: https://github.com/awedwards/DC-Treg-CD8T-interactions-project. Example images of the segmentation and the microniche analysis workflow are provided in Extended Data S1C-F.

Generation of IL-2 and IL-12 fusion proteins

Extended half-life cytokine-MSA fusions were generated as previously described[127,128]. HEK293 cells (at 1 million cells/ml) were transfected with sterile-filtered plasmid DNA (1 mg/L cell culture) using polyethylenimine (2 mg per liter cell culture) in OptiPro serum-free medium (40 ml/L cell culture) (Thermo Fisher). His-tagged proteins were isolated from HEK293 supernatant using TALON Metal Affinity Resin (Takara Bio Inc.). Cytokine-fusion proteins were then further purified by size exclusion chromatography using a HiLoad 16/600 Superdex 200 pg column on an ÄKTA FPLC system (GE Healthcare) that had been pretreated for 4 hours with 1 M NaOH to remove endotoxin and subsequently equilibrated in

sterile PBS (Corning). After purification, all proteins were buffer exchanged into sterile PBS (Corning), 0.2 micron sterile-filtered (Pall Corporation), and confirmed to contain minimal endotoxin (<0.1 EU per injection) usinga chromogenic LAL assay (Lonza). To confirm their molecular weights, proteins were run alongside a Novex Prestaind Sharp Protein Ladder on a 4–12% NuPAGE Bis-Tris protein gel (Life Technologies) with 1% MES running buffer. Proteins were flash-frozen and stored at −80°C, but before therapeutic injection, cytokine fusion proteins were warmed to room temperature.

Cytokine measurements in LN supernatant

LN were homogenized in T-PER Tissue Protein Extraction Reagent (Thermo Fisher Scientific) supplemented with cOmplete™ Protease Inhibitor Cocktail (Sigma-Aldrich) and centrifuged for 5 min at 500 g. LN supernatant was collected, flash-frozen and stored at −80°C. IFNγ and IL-2 cytokines were quantified via ELISA (Mouse IFNγ DuoSet ELISA, R&D Systems; Mouse IL-2 DuoSet ELISA) following manufacturer's instructions.

Seq-Well scRNA-seq

For scRNA-seq of *ex vivo*-primed T cells, $CD8^+$ OT-I T cells and ZsG^+ DC1 sorted from tumor-draining mLN were cultured alone or in the presence of Treg cells sorted from tumor-draining mLN (added at the 1:8 Treg:OT-I ratio) as described above. After the 3-day co-culture, cells were collected for sequencing. For scRNA-seq of Treg cells, LN were mashed through a 70 μm filter into RPMI (GIBCO), then incubated with αCD16/CD32 (clone 93, BioLegend) in FACS buffer (PBS (GIBCO) with 1% FBS (Atlanta Biologicals) and 2 mM EDTA (Invitrogen)) for 15 min at 4°C, washed with FACS buffer and stained with a mix of αCD45-APC (1:200, clone 30-F11, Biolegend) and Total-seq A mouse hashtag antibody (1:100, clone 30-F11, Biolegend) in FACS buffer to label individual mice (hashtag labeling was only performed for tdLN, not naïve LN). Cells were then washed twice in FACS buffer and tdLN cells from multiple mice were pooled together for subsequent $CD4^+$ T cell enrichment sing the mouse $CD4^+$ T cell isolation kit (Miltenyi Biotec), following manufacturer's instructions. Next, cells were stained for FACS and Treg cells were sorted as previously described. Cells from *ex vivo* co-cultures and sorted Treg cells were processed for scRNA-seq using the Seq-Well platform with second strand chemistry, as previously described[129,130]. Whole transcriptome libraries were barcoded and amplified using the Nextera XT kit (Illumina) and were sequenced on a Novaseq 6000 (Illumina). Hashtag oligo libraries were amplified as described previously and were sequenced on a Nextseq 550[131].

Processing of cell hashing data

Cell hashing data was aligned to HTO barcodes using CITE-seq-Count v1.4.2[132]. To establish thresholds for positivity for each HTO barcode, we first performed centered log-ratio normalization of the HTO matrix and then performed k-medoids clustering with k=5 (one for each HTO). This produced consistently five clusters, each dominated by one of the 5 barcodes. For each cluster, we first identified the HTO barcode that was dominant in that cluster. We then considered the threshold to be the lowest value for that HTO barcode among the cells classified in that cluster. To account for the scenario in which this value was substantially lower than the rest of the values in the cluster, we used Grubbs' test to determine whether this threshold was statistically an outlier relative to the rest of the

cluster. If the lower bound was determined to be an outlier at p=0.05, it was removed from the cluster, and the next lowest value was used as the new threshold. This procedure was iteratively applied until the lowest value in the cluster was no longer considered an outlier at p=0.05. Cells were then determined to be "positive" or "negative" for each HTO barcode based on these thresholds. Cells that were positive for multiple HTOs or were negative for all HTOs were excluded from downstream analysis. To account for differences in sequencing depth between samples, these steps were performed separately for each Seq-Well array that was processed.

scRNA-seq data processing and visualization

Raw read processing of scRNA-seq reads was performed as previously described[133]. Briefly, reads were aligned to the mm10 reference genome and collapsed by cell barcode and unique molecular identifier (UMI). Then, cells with less than 1000 (for the co-culture dataset) or 700 (for the Treg cell dataset) unique genes detected and genes detected in fewer than 5 cells were filtered out, and the data for each cell was log-normalized to account for library size. Genes with log-mean expression values greater than 0.1 and a dispersion of greater than 1 were selected as variable genes, and the ScaleData function in Seurat v2.3.4[134] was used to regress out the number of UMI and percentage of mitochondrial genes in each cell. Principal components analysis was performed. The number of principal components used for visualization was determined by examination of the elbow plot, and two-dimensional embeddings were generated using uniform manifold approximation and projection (UMAP). Clusters were determined using Louvain clustering, as implemented in the FindClusters function in Seurat. In the *ex vivo* co-culture dataset, $CD8^+$ T cells were specifically identified based on the expression of canonical $CD8^+$ T cell transcripts including *CD3e*, *CD8a*, *Lck* and *Thy1*, and these $CD8^+$ T cell clusters were selected further analysis. The $CD8^+$ T cells were reprocessed with the same processing and clustering steps described above. DEG analysis was performed for the $CD8^+$ T cells between the two co-culture conditions using the FindMarkers function. Gene signature scores defined as the top 50 DEGs of the *in vivo*-primed $CD8^+$ T cells from tumor-draining mLN and iLN[24] were calculated using Seurat's AddModuleScore function[135] and compared between the two co-culture conditions. In the Treg cell dataset, Treg cells were identified based on the expression of canonical Treg cell transcripts including *CD3e*, *CD4*, *FoxP3* and *Il2ra*, and the contaminating cell clusters were removed. Naïve T cell gene set signature scores[69–71] were obtained from MSigDB[136] and calculated using Seurat's AddModuleScore function[135] and compared across Treg cell clusters. Clusters that contained activated Treg cells were selected for further analysis. These cells were reprocessed with the same processing and clustering steps described above. DEG analysis was performed for each cluster and between indicated cell populations using the FindMarkers function.

Paired single-cell TCR-seq and analysis

Paired TCR-seq and read alignment was performed as previously described[137]. Briefly, whole transcriptome amplification product from each single-cell library was enriched for TCR transcripts using biotinylated *Tcrb* and *Tcra* probes and magnetic streptavidin beads. The enrichment product was further amplified using V-region primers and Nextera sequencing handles, and the resulting libraries were sequenced on an Illumina Novaseq

6000. Processing of reads was performed using the Immcantation software suite[138,139]. Briefly, reads were aggregated by cell barcode and UMI, and UMI with under 10 reads were discarded. ClusterSets.py was used to divide sequences for each UMI into sets of similar sequences. Only sets of sequences that comprised greater than 90% of the sequences obtained for that UMI were considered further. Consensus sequences for each UMI were determined using the BuildConsensus.py function. Consensus sequences were then mapped against TCRV and TCRJ IMGT references sequences with IgBlast. Sequences for which a CDR3 sequence could not be unambiguously determined were discarded. UMI for consensus sequences were corrected using a directional UMI collapse, as implemented in UMI-tools[140]. TCR sequences were then mapped to single cell transcriptomes by matching cell barcodes. If multiple *Tcra* or *Tcrb* sequences were detected for a single cell barcode, then the corresponding sequence with the highest number of UMI and raw reads was retained. Expanded clones were defined as multiple cells from the same mouse (i.e. with same hashtag signal where hashing antibodies were used) containing identical CDR3β junction nucleotide sequences. Clonal size was defined as the number of cells from a given mouse (identified based on the hashtag signal where hashing antibodies were used) that share the same CDR3β junction nucleotide sequence.

Re-analysis of dataset from Sade-Feldman et al. (Cell 2018)

Patient characteristics and scRNA-seq of tumor-infiltrating immune cells from metastatic melanoma patients published by Sade-Feldman *et al.*[103] were downloaded from the Gene Expression Omnibus (GEO, accession GSE120575). This dataset was processed as previously described[141]. Briefly, a Seurat v3.0.0[134] object was created such that the counts slot and data slot were populated with TPM counts and log(TPM+1) counts, respectively. Highly variable genes were identified (FindVariableFeatures) and the data was scaled (ScaleData, while regressing out percentage mitochondrial content per cell and the number of detected reads per cell) followed by dimensionality reduction with PCA using Seurat's standard preprocessing procedure. Clusters were determined using FindNeighbors and FindClusters Seurat functions with 21 principal components (clustering resolution 0.6). Subsequently, hallmark IFN response gene set signature scores[136,142] for cells within the FoxP3$^+$ Treg cell cluster were calculated using Seurat's AddModuleScore function[135] and compared between ICB-responders and non-responders.

QUANTIFICATION AND STATISTICAL ANALYSIS

Statistical analyses were performed using GraphPad Prism (GraphPad) and R. All data are shown as mean ± SEM, unless otherwise indicated. For flow cytometry and immunofluorescence data, statistical analyses were performed with Mann-Whitney U (MWU) test for comparison of two groups, Kruskal-Wallis (KW) test for comparison of more than two groups, or two-way ANOVA for multiple comparisons with *$p < 0.05$; **$p < 0.01$; ***$p < 0.001$; ****$p < 0.0001$; ns=not significant. Nonparametric tests were used as the small sample sizes in our study did not allow us to assume a normal distribution[143]. For scRNA-seq differential gene expression and pathway analyses, p-values were calculated using a two-sided MWU test and adjusted with Bonferroni correction.

Supplementary Material

Refer to Web version on PubMed Central for supplementary material.

ACKNOWLEDGEMENTS

We thank Ömer Yilmaz, Heaji Shin and Andrea Vargas for providing GF mice; Arlene Sharpe (Harvard) and Max Krummel (UCSF) for advice; Ellen Duong, Yash Agarwal, Megan Ruhland (UCSF), Thomas Diefenbach (Ragon) and Peter Savage (UChicago) for experimental guidance; Arjun Bhutkar and Sarah Blatt for assistance with initial processing of the human dataset; Melissa Duquette for mouse colony maintenance and laboratory support; Paul Thompson for administrative support; Koch Institute Swanson Biotechnology Center and the Ragon Institute Microscopy Core for technical support. This work was supported by the Pew Stewart scholarship, the Koch Institute Frontier Research program, the Ludwig Center at MIT and in part by the MIT School of Science Fellowship in Cancer Research.

REFERENCES

1. Fridman WH, Pages F, Sautes-Fridman C, and Galon J (2012). The immune contexture in human tumours: impact on clinical outcome. Nat Rev Cancer 12, 298–306. 10.1038/nrc3245. [PubMed: 22419253]
2. Weigelin B, den Boer AT, Wagena E, Broen K, Dolstra H, de Boer RJ, Figdor CG, Textor J, and Friedl P (2021). Cytotoxic T cells are able to efficiently eliminate cancer cells by additive cytotoxicity. Nat Commun 12, 5217. 10.1038/s41467-021-25282-3. [PubMed: 34471116]
3. Chen DS, and Mellman I (2013). Oncology meets immunology: the cancer-immunity cycle. Immunity 39, 1–10. 10.1016/j.immuni.2013.07.012. [PubMed: 23890059]
4. Hildner K, Edelson BT, Purtha WE, Diamond M, Matsushita H, Kohyama M, Calderon B, Schraml BU, Unanue ER, Diamond MS, et al. (2008). Batf3 deficiency reveals a critical role for CD8alpha+ dendritic cells in cytotoxic T cell immunity. Science 322, 1097–1100. 10.1126/science.1164206. [PubMed: 19008445]
5. Broz ML, Binnewies M, Boldajipour B, Nelson AE, Pollack JL, Erle DJ, Barczak A, Rosenblum MD, Daud A, Barber DL, et al. (2014). Dissecting the Tumor Myeloid Compartment Reveals Rare Activating Antigen-Presenting Cells Critical for T Cell Immunity. Cancer Cell 26, 938. 10.1016/j.ccell.2014.11.010.
6. Lanzavecchia A, and Sallusto F (2001). Regulation of T cell immunity by dendritic cells. Cell 106, 263–266. 10.1016/s0092-8674(01)00455-x. [PubMed: 11509174]
7. den Haan JM, Lehar SM, and Bevan MJ (2000). CD8(+) but not CD8(−) dendritic cells cross-prime cytotoxic T cells in vivo. J Exp Med 192, 1685–1696. 10.1084/jem.192.12.1685. [PubMed: 11120766]
8. De Plaen E, Lurquin C, Van Pel A, Mariame B, Szikora JP, Wolfel T, Sibille C, Chomez P, and Boon T (1988). Immunogenic (tum-) variants of mouse tumor P815: cloning of the gene of tum- antigen P91A and identification of the tum- mutation. Proc Natl Acad Sci U S A 85, 2274–2278. 10.1073/pnas.85.7.2274. [PubMed: 3127830]
9. Inaba K, Witmer-Pack M, Inaba M, Hathcock KS, Sakuta H, Azuma M, Yagita H, Okumura K, Linsley PS, Ikehara S, et al. (1994). The tissue distribution of the B7–2 costimulator in mice: abundant expression on dendritic cells in situ and during maturation in vitro. J Exp Med 180, 1849–1860. 10.1084/jem.180.5.1849. [PubMed: 7525841]
10. Caux C, Vanbervliet B, Massacrier C, Azuma M, Okumura K, Lanier LL, and Banchereau J (1994). B70/B7–2 is identical to CD86 and is the major functional ligand for CD28 expressed on human dendritic cells. J Exp Med 180, 1841–1847. 10.1084/jem.180.5.1841. [PubMed: 7525840]
11. Deeths MJ, and Mescher MF (1997). B7–1-dependent co-stimulation results in qualitatively and quantitatively different responses by CD4+ and CD8+ T cells. Eur J Immunol 27, 598–608. 10.1002/eji.1830270305. [PubMed: 9079798]
12. Harding FA, McArthur JG, Gross JA, Raulet DH, and Allison JP (1992). CD28-mediated signalling co-stimulates murine T cells and prevents induction of anergy in T-cell clones. Nature 356, 607–609. 10.1038/356607a0. [PubMed: 1313950]

13. Jenkins MK, Ashwell JD, and Schwartz RH (1988). Allogeneic non-T spleen cells restore the responsiveness of normal T cell clones stimulated with antigen and chemically modified antigen-presenting cells. J Immunol 140, 3324–3330. [PubMed: 2834436]

14. Cella M, Scheidegger D, Palmer-Lehmann K, Lane P, Lanzavecchia A, and Alber G (1996). Ligation of CD40 on dendritic cells triggers production of high levels of interleukin-12 and enhances T cell stimulatory capacity: T-T help via APC activation. J Exp Med 184, 747–752. 10.1084/jem.184.2.747. [PubMed: 8760829]

15. Le Bon A, Etchart N, Rossmann C, Ashton M, Hou S, Gewert D, Borrow P, and Tough DF (2003). Cross-priming of CD8+ T cells stimulated by virus-induced type I interferon. Nat Immunol 4, 1009–1015. 10.1038/ni978. [PubMed: 14502286]

16. Curtsinger JM, Schmidt CS, Mondino A, Lins DC, Kedl RM, Jenkins MK, and Mescher MF (1999). Inflammatory cytokines provide a third signal for activation of naive CD4+ and CD8+ T cells. J Immunol 162, 3256–3262. [PubMed: 10092777]

17. Fuertes MB, Kacha AK, Kline J, Woo SR, Kranz DM, Murphy KM, and Gajewski TF (2011). Host type I IFN signals are required for antitumor CD8+ T cell responses through CD8{alpha}+ dendritic cells. J Exp Med 208, 2005–2016. 10.1084/jem.20101159. [PubMed: 21930765]

18. Curtsinger JM, Lins DC, and Mescher MF (2003). Signal 3 determines tolerance versus full activation of naive CD8 T cells: dissociating proliferation and development of effector function. J Exp Med 197, 1141–1151. 10.1084/jem.20021910. [PubMed: 12732656]

19. Hernandez J, Aung S, Marquardt K, and Sherman LA (2002). Uncoupling of proliferative potential and gain of effector function by CD8(+) T cells responding to self-antigens. J Exp Med 196, 323–333. 10.1084/jem.20011612. [PubMed: 12163561]

20. Gett AV, Sallusto F, Lanzavecchia A, and Geginat J (2003). T cell fitness determined by signal strength. Nat Immunol 4, 355–360. 10.1038/ni908. [PubMed: 12640450]

21. van Stipdonk MJ, Hardenberg G, Bijker MS, Lemmens EE, Droin NM, Green DR, and Schoenberger SP (2003). Dynamic programming of CD8+ T lymphocyte responses. Nat Immunol 4, 361–365. 10.1038/ni912. [PubMed: 12640451]

22. D'Souza WN, and Hedrick SM (2006). Cutting edge: latecomer CD8 T cells are imprinted with a unique differentiation program. J Immunol 177, 777–781. 10.4049/jimmunol.177.2.777. [PubMed: 16818730]

23. Khan O, Giles JR, McDonald S, Manne S, Ngiow SF, Patel KP, Werner MT, Huang AC, Alexander KA, Wu JE, et al. (2019). TOX transcriptionally and epigenetically programs CD8(+) T cell exhaustion. Nature 571, 211–218. 10.1038/s41586-019-1325-x. [PubMed: 31207603]

24. Horton BL, Morgan DM, Momin N, Zagorulya M, Torres-Mejia E, Bhandarkar V, Wittrup KD, Love JC, and Spranger S (2021). Lack of CD8(+) T cell effector differentiation during priming mediates checkpoint blockade resistance in non-small cell lung cancer. Sci Immunol 6, eabi8800. 10.1126/sciimmunol.abi8800. [PubMed: 34714687]

25. Zagorulya M, and Spranger S (2022). Once upon a prime: DCs shape cancer immunity. Trends Cancer 10.1016/j.trecan.2022.10.006.

26. Romani N, Koide S, Crowley M, Witmer-Pack M, Livingstone AM, Fathman CG, Inaba K, and Steinman RM (1989). Presentation of exogenous protein antigens by dendritic cells to T cell clones. Intact protein is presented best by immature, epidermal Langerhans cells. J Exp Med 169, 1169–1178. 10.1084/jem.169.3.1169. [PubMed: 2522497]

27. De Smedt T, Pajak B, Muraille E, Lespagnard L, Heinen E, De Baetselier P, Urbain J, Leo O, and Moser M (1996). Regulation of dendritic cell numbers and maturation by lipopolysaccharide in vivo. J Exp Med 184, 1413–1424. 10.1084/jem.184.4.1413. [PubMed: 8879213]

28. Dalod M, Salazar-Mather TP, Malmgaard L, Lewis C, Asselin-Paturel C, Briere F, Trinchieri G, and Biron CA (2002). Interferon alpha/beta and interleukin 12 responses to viral infections: pathways regulating dendritic cell cytokine expression in vivo. J Exp Med 195, 517–528. 10.1084/jem.20011672. [PubMed: 11854364]

29. Reis e Sousa C, Hieny S, Scharton-Kersten T, Jankovic D, Charest H, Germain RN, and Sher A (1997). In vivo microbial stimulation induces rapid CD40 ligand-independent production of interleukin 12 by dendritic cells and their redistribution to T cell areas. J Exp Med 186, 1819–1829. 10.1084/jem.186.11.1819. [PubMed: 9382881]

30. Hawiger D, Inaba K, Dorsett Y, Guo M, Mahnke K, Rivera M, Ravetch JV, Steinman RM, and Nussenzweig MC (2001). Dendritic cells induce peripheral T cell unresponsiveness under steady state conditions in vivo. J Exp Med 194, 769–779. 10.1084/jem.194.6.769. [PubMed: 11560993]

31. Bonifaz L, Bonnyay D, Mahnke K, Rivera M, Nussenzweig MC, and Steinman RM (2002). Efficient targeting of protein antigen to the dendritic cell receptor DEC-205 in the steady state leads to antigen presentation on major histocompatibility complex class I products and peripheral CD8+ T cell tolerance. J Exp Med 196, 1627–1638. 10.1084/jem.20021598. [PubMed: 12486105]

32. Liu K, Iyoda T, Saternus M, Kimura Y, Inaba K, and Steinman RM (2002). Immune tolerance after delivery of dying cells to dendritic cells in situ. J Exp Med 196, 1091–1097. 10.1084/jem.20021215. [PubMed: 12391020]

33. Onishi Y, Fehervari Z, Yamaguchi T, and Sakaguchi S (2008). Foxp3+ natural regulatory T cells preferentially form aggregates on dendritic cells in vitro and actively inhibit their maturation. Proc Natl Acad Sci U S A 105, 10113–10118. 10.1073/pnas.0711106105. [PubMed: 18635688]

34. Gu P, Gao JF, D'Souza CA, Kowalczyk A, Chou KY, and Zhang L (2012). Trogocytosis of CD80 and CD86 by induced regulatory T cells. Cell Mol Immunol 9, 136–146. 10.1038/cmi.2011.62. [PubMed: 22307040]

35. Qureshi OS, Zheng Y, Nakamura K, Attridge K, Manzotti C, Schmidt EM, Baker J, Jeffery LE, Kaur S, Briggs Z, et al. (2011). Trans-endocytosis of CD80 and CD86: a molecular basis for the cell-extrinsic function of CTLA-4. Science 332, 600–603. 10.1126/science.1202947. [PubMed: 21474713]

36. Mavin E, Nicholson L, Rafez Ahmed S, Gao F, Dickinson A, and Wang XN (2017). Human Regulatory T Cells Mediate Transcriptional Modulation of Dendritic Cell Function. J Immunol 198, 138–146. 10.4049/jimmunol.1502487. [PubMed: 27895173]

37. Binnewies M, Mujal AM, Pollack JL, Combes AJ, Hardison EA, Barry KC, Tsui J, Ruhland MK, Kersten K, Abushawish MA, et al. (2019). Unleashing Type-2 Dendritic Cells to Drive Protective Antitumor CD4(+) T Cell Immunity. Cell 177, 556–571 e516. 10.1016/j.cell.2019.02.005. [PubMed: 30955881]

38. Bauer CA, Kim EY, Marangoni F, Carrizosa E, Claudio NM, and Mempel TR (2014). Dynamic Treg interactions with intratumoral APCs promote local CTL dysfunction. J Clin Invest 124, 2425–2440. 10.1172/JCI66375. [PubMed: 24812664]

39. Marangoni F, Zhakyp A, Corsini M, Geels SN, Carrizosa E, Thelen M, Mani V, Prussmann JN, Warner RD, Ozga AJ, et al. (2021). Expansion of tumor-associated Treg cells upon disruption of a CTLA-4-dependent feedback loop. Cell 184, 3998–4015 e3919. 10.1016/j.cell.2021.05.027. [PubMed: 34157302]

40. Jang JE, Hajdu CH, Liot C, Miller G, Dustin ML, and Bar-Sagi D (2017). Crosstalk between Regulatory T Cells and Tumor-Associated Dendritic Cells Negates Anti-tumor Immunity in Pancreatic Cancer. Cell Rep 20, 558–571. 10.1016/j.celrep.2017.06.062. [PubMed: 28723561]

41. Joshi NS, Akama-Garren EH, Lu Y, Lee DY, Chang GP, Li A, DuPage M, Tammela T, Kerper NR, Farago AF, et al. (2015). Regulatory T Cells in Tumor-Associated Tertiary Lymphoid Structures Suppress Anti-tumor T Cell Responses. Immunity 43, 579–590. 10.1016/j.immuni.2015.08.006. [PubMed: 26341400]

42. Poholek AC (2021). Tissue-Specific Contributions to Control of T Cell Immunity. Immunohorizons 5, 410–423. 10.4049/immunohorizons.2000103. [PubMed: 34103371]

43. Mikhak Z, Strassner JP, and Luster AD (2013). Lung dendritic cells imprint T cell lung homing and promote lung immunity through the chemokine receptor CCR4. J Exp Med 210, 1855–1869. 10.1084/jem.20130091. [PubMed: 23960189]

44. Kim TS, Gorski SA, Hahn S, Murphy KM, and Braciale TJ (2014). Distinct dendritic cell subsets dictate the fate decision between effector and memory CD8(+) T cell differentiation by a CD24-dependent mechanism. Immunity 40, 400–413. 10.1016/j.immuni.2014.02.004. [PubMed: 24631155]

45. Svensson M, Johansson-Lindbom B, Zapata F, Jaensson E, Austenaa LM, Blomhoff R, and Agace WW (2008). Retinoic acid receptor signaling levels and antigen dose regulate gut homing receptor expression on CD8+ T cells. Mucosal Immunol 1, 38–48. 10.1038/mi.2007.4. [PubMed: 19079159]

46. Esterhazy D, Canesso MCC, Mesin L, Muller PA, de Castro TBR, Lockhart A, ElJalby M, Faria AMC, and Mucida D (2019). Compartmentalized gut lymph node drainage dictates adaptive immune responses. Nature 569, 126–130. 10.1038/s41586-019-1125-3. [PubMed: 30988509]
47. Mani V, Bromley SK, Aijo T, Mora-Buch R, Carrizosa E, Warner RD, Hamze M, Sen DR, Chasse AY, Lorant A, et al. (2019). Migratory DCs activate TGF-beta to precondition naive CD8(+) T cells for tissue-resident memory fate. Science 366. 10.1126/science.aav5728.
48. Leal JM, Huang JY, Kohli K, Stoltzfus C, Lyons-Cohen MR, Olin BE, Gale M Jr., and Gerner MY (2021). Innate cell microenvironments in lymph nodes shape the generation of T cell responses during type I inflammation. Sci Immunol 6. 10.1126/sciimmunol.abb9435.
49. Duckworth BC, Lafouresse F, Wimmer VC, Broomfield BJ, Dalit L, Alexandre YO, Sheikh AA, Qin RZ, Alvarado C, Mielke LA, et al. (2021). Effector and stem-like memory cell fates are imprinted in distinct lymph node niches directed by CXCR3 ligands. Nat Immunol 22, 434–448. 10.1038/s41590-021-00878-5. [PubMed: 33649580]
50. LaFave LM, Kartha VK, Ma S, Meli K, Del Priore I, Lareau C, Naranjo S, Westcott PMK, Duarte FM, Sankar V, et al. (2020). Epigenomic State Transitions Characterize Tumor Progression in Mouse Lung Adenocarcinoma. Cancer Cell 38, 212–228 e213. 10.1016/j.ccell.2020.06.006. [PubMed: 32707078]
51. Roberts EW, Broz ML, Binnewies M, Headley MB, Nelson AE, Wolf DM, Kaisho T, Bogunovic D, Bhardwaj N, and Krummel MF (2016). Critical Role for CD103(+)/CD141(+) Dendritic Cells Bearing CCR7 for Tumor Antigen Trafficking and Priming of T Cell Immunity in Melanoma. Cancer Cell 30, 324–336. 10.1016/j.ccell.2016.06.003. [PubMed: 27424807]
52. Yamazaki C, Sugiyama M, Ohta T, Hemmi H, Hamada E, Sasaki I, Fukuda Y, Yano T, Nobuoka M, Hirashima T, et al. (2013). Critical roles of a dendritic cell subset expressing a chemokine receptor, XCR1. J Immunol 190, 6071–6082. 10.4049/jimmunol.1202798. [PubMed: 23670193]
53. Duong E, Fessenden TB, Lutz E, Dinter T, Yim L, Blatt S, Bhutkar A, Wittrup KD, and Spranger S (2022). Type I interferon activates MHC class I-dressed CD11b(+) conventional dendritic cells to promote protective anti-tumor CD8(+) T cell immunity. Immunity 55, 308–323 e309. 10.1016/j.immuni.2021.10.020. [PubMed: 34800368]
54. Maier B, Leader AM, Chen ST, Tung N, Chang C, LeBerichel J, Chudnovskiy A, Maskey S, Walker L, Finnigan JP, et al. (2020). A conserved dendritic-cell regulatory program limits antitumour immunity. Nature 580, 257–262. 10.1038/s41586-020-2134-y. [PubMed: 32269339]
55. Sallusto F, Schaerli P, Loetscher P, Schaniel C, Lenig D, Mackay CR, Qin S, and Lanzavecchia A (1998). Rapid and coordinated switch in chemokine receptor expression during dendritic cell maturation. Eur J Immunol 28, 2760–2769. 10.1002/(SICI)1521-4141(199809)28:09<2760::AID-IMMU2760>3.0.CO;2-N. [PubMed: 9754563]
56. Cella M, Engering A, Pinet V, Pieters J, and Lanzavecchia A (1997). Inflammatory stimuli induce accumulation of MHC class II complexes on dendritic cells. Nature 388, 782–787. 10.1038/42030. [PubMed: 9285591]
57. Fontenot JD, Gavin MA, and Rudensky AY (2003). Foxp3 programs the development and function of CD4+CD25+ regulatory T cells. Nat Immunol 4, 330–336. 10.1038/ni904. [PubMed: 12612578]
58. Chen Z, Ji Z, Ngiow SF, Manne S, Cai Z, Huang AC, Johnson J, Staupe RP, Bengsch B, Xu C, et al. (2019). TCF-1-Centered Transcriptional Network Drives an Effector versus Exhausted CD8 T Cell-Fate Decision. Immunity 51, 840–855 e845. 10.1016/j.immuni.2019.09.013. [PubMed: 31606264]
59. Pipkin ME, Sacks JA, Cruz-Guilloty F, Lichtenheld MG, Bevan MJ, and Rao A (2010). Interleukin-2 and inflammation induce distinct transcriptional programs that promote the differentiation of effector cytolytic T cells. Immunity 32, 79–90. 10.1016/j.immuni.2009.11.012. [PubMed: 20096607]
60. Kalia V, Sarkar S, Subramaniam S, Haining WN, Smith KA, and Ahmed R (2010). Prolonged interleukin-2Ralpha expression on virus-specific CD8+ T cells favors terminal-effector differentiation in vivo. Immunity 32, 91–103. 10.1016/j.immuni.2009.11.010. [PubMed: 20096608]
61. Marelli-Berg FM, Clement M, Mauro C, and Caligiuri G (2013). An immunologist's guide to CD31 function in T-cells. J Cell Sci 126, 2343–2352. 10.1242/jcs.124099. [PubMed: 23761922]

62. Xing S, Li F, Zeng Z, Zhao Y, Yu S, Shan Q, Li Y, Phillips FC, Maina PK, Qi HH, et al. (2016). Tcf1 and Lef1 transcription factors establish CD8(+) T cell identity through intrinsic HDAC activity. Nat Immunol 17, 695–703. 10.1038/ni.3456. [PubMed: 27111144]
63. Dorsam G, Graeler MH, Seroogy C, Kong Y, Voice JK, and Goetzl EJ (2003). Transduction of multiple effects of sphingosine 1-phosphate (S1P) on T cell functions by the S1P1 G protein-coupled receptor. J Immunol 171, 3500–3507. 10.4049/jimmunol.171.7.3500. [PubMed: 14500646]
64. Hart GT, Hogquist KA, and Jameson SC (2012). Kruppel-like factors in lymphocyte biology. J Immunol 188, 521–526. 10.4049/jimmunol.1101530. [PubMed: 22223851]
65. Garris CS, Arlauckas SP, Kohler RH, Trefny MP, Garren S, Piot C, Engblom C, Pfirschke C, Siwicki M, Gungabeesoon J, et al. (2018). Successful Anti-PD-1 Cancer Immunotherapy Requires T Cell-Dendritic Cell Crosstalk Involving the Cytokines IFN-gamma and IL-12. Immunity 49, 1148–1161 e1147. 10.1016/j.immuni.2018.09.024. [PubMed: 30552023]
66. Saleh R, and Elkord E (2020). FoxP3(+) T regulatory cells in cancer: Prognostic biomarkers and therapeutic targets. Cancer Lett 490, 174–185. 10.1016/j.canlet.2020.07.022. [PubMed: 32721551]
67. Gubser C, Schmaler M, Rossi SW, and Palmer E (2016). Monoclonal regulatory T cells provide insights into T cell suppression. Sci Rep 6, 25758. 10.1038/srep25758. [PubMed: 27210828]
68. Shevyrev D, and Tereshchenko V (2019). Treg Heterogeneity, Function, and Homeostasis. Front Immunol 10, 3100. 10.3389/fimmu.2019.03100. [PubMed: 31993063]
69. Miyara M, Yoshioka Y, Kitoh A, Shima T, Wing K, Niwa A, Parizot C, Taflin C, Heike T, Valeyre D, et al. (2009). Functional delineation and differentiation dynamics of human CD4+ T cells expressing the FoxP3 transcription factor. Immunity 30, 899–911. 10.1016/j.immuni.2009.03.019. [PubMed: 19464196]
70. Wei G, Wei L, Zhu J, Zang C, Hu-Li J, Yao Z, Cui K, Kanno Y, Roh TY, Watford WT, et al. (2009). Global mapping of H3K4me3 and H3K27me3 reveals specificity and plasticity in lineage fate determination of differentiating CD4+ T cells. Immunity 30, 155–167. 10.1016/j.immuni.2008.12.009. [PubMed: 19144320]
71. Abbas AR, Wolslegel K, Seshasayee D, Modrusan Z, and Clark HF (2009). Deconvolution of blood microarray data identifies cellular activation patterns in systemic lupus erythematosus. PLoS One 4, e6098. 10.1371/journal.pone.0006098. [PubMed: 19568420]
72. Zemmour D, Zilionis R, Kiner E, Klein AM, Mathis D, and Benoist C (2018). Single-cell gene expression reveals a landscape of regulatory T cell phenotypes shaped by the TCR. Nat Immunol 19, 291–301. 10.1038/s41590-018-0051-0. [PubMed: 29434354]
73. Miragaia RJ, Gomes T, Chomka A, Jardine L, Riedel A, Hegazy AN, Whibley N, Tucci A, Chen X, Lindeman I, et al. (2019). Single-Cell Transcriptomics of Regulatory T Cells Reveals Trajectories of Tissue Adaptation. Immunity 50, 493–504 e497. 10.1016/j.immuni.2019.01.001. [PubMed: 30737144]
74. Hori S, Haury M, Coutinho A, and Demengeot J (2002). Specificity requirements for selection and effector functions of CD25+4+ regulatory T cells in anti-myelin basic protein T cell receptor transgenic mice. Proc Natl Acad Sci U S A 99, 8213–8218. 10.1073/pnas.122224799. [PubMed: 12034883]
75. Tarbell KV, Yamazaki S, Olson K, Toy P, and Steinman RM (2004). CD25+ CD4+ T cells, expanded with dendritic cells presenting a single autoantigenic peptide, suppress autoimmune diabetes. J Exp Med 199, 1467–1477. 10.1084/jem.20040180. [PubMed: 15184500]
76. Plitas G, Konopacki C, Wu K, Bos PD, Morrow M, Putintseva EV, Chudakov DM, and Rudensky AY (2016). Regulatory T Cells Exhibit Distinct Features in Human Breast Cancer. Immunity 45, 1122–1134. 10.1016/j.immuni.2016.10.032. [PubMed: 27851913]
77. Malchow S, Leventhal DS, Nishi S, Fischer BI, Shen L, Paner GP, Amit AS, Kang C, Geddes JE, Allison JP, et al. (2013). Aire-dependent thymic development of tumor-associated regulatory T cells. Science 339, 1219–1224. 10.1126/science.1233913. [PubMed: 23471412]
78. Zheng C, Zheng L, Yoo JK, Guo H, Zhang Y, Guo X, Kang B, Hu R, Huang JY, Zhang Q, et al. (2017). Landscape of Infiltrating T Cells in Liver Cancer Revealed by Single-Cell Sequencing. Cell 169, 1342–1356 e1316. 10.1016/j.cell.2017.05.035. [PubMed: 28622514]

79. Delgoffe GM, Woo SR, Turnis ME, Gravano DM, Guy C, Overacre AE, Bettini ML, Vogel P, Finkelstein D, Bonnevier J, et al. (2013). Stability and function of regulatory T cells is maintained by a neuropilin-1-semaphorin-4a axis. Nature 501, 252–256. 10.1038/nature12428. [PubMed: 23913274]
80. Stagg J, Divisekera U, Duret H, Sparwasser T, Teng MW, Darcy PK, and Smyth MJ (2011). CD73-deficient mice have increased antitumor immunity and are resistant to experimental metastasis. Cancer Res 71, 2892–2900. 10.1158/0008-5472.CAN-10-4246. [PubMed: 21292811]
81. Shalev I, Liu H, Koscik C, Bartczak A, Javadi M, Wong KM, Maknojia A, He W, Liu MF, Diao J, et al. (2008). Targeted deletion of fgl2 leads to impaired regulatory T cell activity and development of autoimmune glomerulonephritis. J Immunol 180, 249–260. 10.4049/jimmunol.180.1.249. [PubMed: 18097026]
82. Koch MA, Tucker-Heard G, Perdue NR, Killebrew JR, Urdahl KB, and Campbell DJ (2009). The transcription factor T-bet controls regulatory T cell homeostasis and function during type 1 inflammation. Nat Immunol 10, 595–602. 10.1038/ni.1731. [PubMed: 19412181]
83. Condino-Neto A, and Newburger PE (2000). Interferon-gamma improves splicing efficiency of CYBB gene transcripts in an interferon-responsive variant of chronic granulomatous disease due to a splice site consensus region mutation. Blood 95, 3548–3554. [PubMed: 10828042]
84. You M, Yu DH, and Feng GS (1999). Shp-2 tyrosine phosphatase functions as a negative regulator of the interferon-stimulated Jak/STAT pathway. Mol Cell Biol 19, 2416–2424. 10.1128/MCB.19.3.2416. [PubMed: 10022928]
85. Perkey E, Maurice De Sousa D, Carrington L, Chung J, Dils A, Granadier D, Koch U, Radtke F, Ludewig B, Blazar BR, et al. (2020). GCNT1-Mediated O-Glycosylation of the Sialomucin CD43 Is a Sensitive Indicator of Notch Signaling in Activated T Cells. J Immunol 204, 1674–1688. 10.4049/jimmunol.1901194. [PubMed: 32060138]
86. Hutloff A, Dittrich AM, Beier KC, Eljaschewitsch B, Kraft R, Anagnostopoulos I, and Kroczek RA (1999). ICOS is an inducible T-cell co-stimulator structurally and functionally related to CD28. Nature 397, 263–266. 10.1038/16717. [PubMed: 9930702]
87. Kakugawa K, Kojo S, Tanaka H, Seo W, Endo TA, Kitagawa Y, Muroi S, Tenno M, Yasmin N, Kohwi Y, et al. (2017). Essential Roles of SATB1 in Specifying T Lymphocyte Subsets. Cell Rep 19, 1176–1188. 10.1016/j.celrep.2017.04.038. [PubMed: 28494867]
88. Kashiwakura Y, Sakurai D, Kanno Y, Hashiguchi M, Kobayashi A, Kurosu A, Tokudome S, Kobata T, and Kojima H (2013). CD2-mediated regulation of peripheral CD4(+) CD25(+) regulatory T-cell apoptosis accompanied by down-regulation of Bim. Immunology 139, 48–60. 10.1111/imm.12054. [PubMed: 23278598]
89. Li A, Herbst RH, Canner D, Schenkel JM, Smith OC, Kim JY, Hillman M, Bhutkar A, Cuoco MS, Rappazzo CG, et al. (2019). IL-33 Signaling Alters Regulatory T Cell Diversity in Support of Tumor Development. Cell Rep 29, 2998–3008 e2998. 10.1016/j.celrep.2019.10.120. [PubMed: 31801068]
90. Halim L, Romano M, McGregor R, Correa I, Pavlidis P, Grageda N, Hoong SJ, Yuksel M, Jassem W, Hannen RF, et al. (2017). An Atlas of Human Regulatory T Helper-like Cells Reveals Features of Th2-like Tregs that Support a Tumorigenic Environment. Cell Rep 20, 757–770. 10.1016/j.celrep.2017.06.079. [PubMed: 28723576]
91. Huang S, Hendriks W, Althage A, Hemmi S, Bluethmann H, Kamijo R, Vilcek J, Zinkernagel RM, and Aguet M (1993). Immune response in mice that lack the interferon-gamma receptor. Science 259, 1742–1745. 10.1126/science.8456301. [PubMed: 8456301]
92. Muller U, Steinhoff U, Reis LF, Hemmi S, Pavlovic J, Zinkernagel RM, and Aguet M (1994). Functional role of type I and type II interferons in antiviral defense. Science 264, 1918–1921. 10.1126/science.8009221. [PubMed: 8009221]
93. Bradley KC, Finsterbusch K, Schnepf D, Crotta S, Llorian M, Davidson S, Fuchs SY, Staeheli P, and Wack A (2019). Microbiota-Driven Tonic Interferon Signals in Lung Stromal Cells Protect from Influenza Virus Infection. Cell Rep 28, 245–256 e244. 10.1016/j.celrep.2019.05.105. [PubMed: 31269444]
94. Maurice NJ, McElrath MJ, Andersen-Nissen E, Frahm N, and Prlic M (2019). CXCR3 enables recruitment and site-specific bystander activation of memory CD8(+) T cells. Nat Commun 10, 4987. 10.1038/s41467-019-12980-2. [PubMed: 31676770]

95. Bangs DJ, Tsitsiklis A, Steier Z, Chan SW, Kaminski J, Streets A, Yosef N, and Robey EA (2022). CXCR3 regulates stem and proliferative CD8+ T cells during chronic infection by promoting interactions with DCs in splenic bridging channels. Cell Rep 38, 110266. 10.1016/j.celrep.2021.110266. [PubMed: 35045305]

96. Groom JR, Richmond J, Murooka TT, Sorensen EW, Sung JH, Bankert K, von Andrian UH, Moon JJ, Mempel TR, and Luster AD (2012). CXCR3 chemokine receptor-ligand interactions in the lymph node optimize CD4+ T helper 1 cell differentiation. Immunity 37, 1091–1103. 10.1016/j.immuni.2012.08.016. [PubMed: 23123063]

97. Rapp M, Wintergerst MWM, Kunz WG, Vetter VK, Knott MML, Lisowski D, Haubner S, Moder S, Thaler R, Eiber S, et al. (2019). CCL22 controls immunity by promoting regulatory T cell communication with dendritic cells in lymph nodes. J Exp Med 216, 1170–1181. 10.1084/jem.20170277. [PubMed: 30910796]

98. Coghill JM, Fowler KA, West ML, Fulton LM, van Deventer H, McKinnon KP, Vincent BG, Lin K, Panoskaltsis-Mortari A, Cook DN, et al. (2013). CC chemokine receptor 8 potentiates donor Treg survival and is critical for the prevention of murine graft-versus-host disease. Blood 122, 825–836. 10.1182/blood-2012-06-435735. [PubMed: 23798714]

99. Muthuswamy R, Urban J, Lee JJ, Reinhart TA, Bartlett D, and Kalinski P (2008). Ability of mature dendritic cells to interact with regulatory T cells is imprinted during maturation. Cancer Res 68, 5972–5978. 10.1158/0008-5472.CAN-07-6818. [PubMed: 18632653]

100. Curtsinger JM, Agarwal P, Lins DC, and Mescher MF (2012). Autocrine IFN-gamma promotes naive CD8 T cell differentiation and synergizes with IFN-alpha to stimulate strong function. J Immunol 189, 659–668. 10.4049/jimmunol.1102727. [PubMed: 22706089]

101. Tau GZ, Cowan SN, Weisburg J, Braunstein NS, and Rothman PB (2001). Regulation of IFN-gamma signaling is essential for the cytotoxic activity of CD8(+) T cells. J Immunol 167, 5574–5582. 10.4049/jimmunol.167.10.5574. [PubMed: 11698428]

102. Bhat P, Leggatt G, Waterhouse N, and Frazer IH (2017). Interferon-gamma derived from cytotoxic lymphocytes directly enhances their motility and cytotoxicity. Cell Death Dis 8, e2836. 10.1038/cddis.2017.67. [PubMed: 28569770]

103. Sade-Feldman M, Yizhak K, Bjorgaard SL, Ray JP, de Boer CG, Jenkins RW, Lieb DJ, Chen JH, Frederick DT, Barzily-Rokni M, et al. (2018). Defining T Cell States Associated with Response to Checkpoint Immunotherapy in Melanoma. Cell 175, 998–1013 e1020. 10.1016/j.cell.2018.10.038. [PubMed: 30388456]

104. Horton BL, Fessenden TB, and Spranger S (2019). Tissue Site and the Cancer Immunity Cycle. Trends Cancer 5, 593–603. 10.1016/j.trecan.2019.07.006. [PubMed: 31706507]

105. Zagorulya M, Duong E, and Spranger S (2020). Impact of anatomic site on antigen-presenting cells in cancer. J Immunother Cancer 8. 10.1136/jitc-2020-001204.

106. Tan TG, Mathis D, and Benoist C (2016). Singular role for T-BET+CXCR3+ regulatory T cells in protection from autoimmune diabetes. Proc Natl Acad Sci U S A 113, 14103–14108. 10.1073/pnas.1616710113. [PubMed: 27872297]

107. Choi J, Ziga ED, Ritchey J, Collins L, Prior JL, Cooper ML, Piwnica-Worms D, and DiPersio JF (2012). IFNgammaR signaling mediates alloreactive T-cell trafficking and GVHD. Blood 120, 4093–4103. 10.1182/blood-2012-01-403196. [PubMed: 22972985]

108. Levine AG, Mendoza A, Hemmers S, Moltedo B, Niec RE, Schizas M, Hoyos BE, Putintseva EV, Chaudhry A, Dikiy S, et al. (2017). Stability and function of regulatory T cells expressing the transcription factor T-bet. Nature 546, 421–425. 10.1038/nature22360. [PubMed: 28607488]

109. Lee JC, Mehdizadeh S, Smith J, Young A, Mufazalov IA, Mowery CT, Daud A, and Bluestone JA (2020). Regulatory T cell control of systemic immunity and immunotherapy response in liver metastasis. Sci Immunol 5. 10.1126/sciimmunol.aba0759.

110. Huffnagle GB, Dickson RP, and Lukacs NW (2017). The respiratory tract microbiome and lung inflammation: a two-way street. Mucosal Immunol 10, 299–306. 10.1038/mi.2016.108. [PubMed: 27966551]

111. Ramirez-Labrada AG, Isla D, Artal A, Arias M, Rezusta A, Pardo J, and Galvez EM (2020). The Influence of Lung Microbiota on Lung Carcinogenesis, Immunity, and Immunotherapy. Trends Cancer 6, 86–97. 10.1016/j.trecan.2019.12.007. [PubMed: 32061309]

112. Lee N, and Kim WU (2017). Microbiota in T-cell homeostasis and inflammatory diseases. Exp Mol Med 49, e340. 10.1038/emm.2017.36. [PubMed: 28546563]
113. Ansaldo E, Farley TK, and Belkaid Y (2021). Control of Immunity by the Microbiota. Annu Rev Immunol 39, 449–479. 10.1146/annurev-immunol-093019-112348. [PubMed: 33902310]
114. Tastan C, Karhan E, Zhou W, Fleming E, Voigt AY, Yao X, Wang L, Horne M, Placek L, Kozhaya L, et al. (2018). Tuning of human MAIT cell activation by commensal bacteria species and MR1-dependent T-cell presentation. Mucosal Immunol 11, 1591–1605. 10.1038/s41385-018-0072-x. [PubMed: 30115998]
115. Ataide MA, Knopper K, Cruz de Casas P, Ugur M, Eickhoff S, Zou M, Shaikh H, Trivedi A, Grafen A, Yang T, et al. (2022). Lymphatic migration of unconventional T cells promotes site-specific immunity in distinct lymph nodes. Immunity. 10.1016/j.immuni.2022.07.019.
116. Sullivan MR, Danai LV, Lewis CA, Chan SH, Gui DY, Kunchok T, Dennstedt EA, Vander Heiden MG, and Muir A (2019). Quantification of microenvironmental metabolites in murine cancers reveals determinants of tumor nutrient availability. Elife 8. 10.7554/eLife.44235.
117. Feng Q, Liu Z, Yu X, Huang T, Chen J, Wang J, Wilhelm J, Li S, Song J, Li W, et al. (2022). Lactate increases stemness of CD8 + T cells to augment anti-tumor immunity. Nat Commun 13, 4981. 10.1038/s41467-022-32521-8. [PubMed: 36068198]
118. Best SA, Gubser PM, Sethumadhavan S, Kersbergen A, Negron Abril YL, Goldford J, Sellers K, Abeysekera W, Garnham AL, McDonald JA, et al. (2022). Glutaminase inhibition impairs CD8 T cell activation in STK11-/Lkb1-deficient lung cancer. Cell Metab 34, 874–887 e876. 10.1016/j.cmet.2022.04.003. [PubMed: 35504291]
119. Zhao S, Peralta RM, Avina-Ochoa N, Delgoffe GM, and Kaech SM (2021). Metabolic regulation of T cells in the tumor microenvironment by nutrient availability and diet. Semin Immunol 52, 101485. 10.1016/j.smim.2021.101485. [PubMed: 34462190]
120. Peng X, He Y, Huang J, Tao Y, and Liu S (2021). Metabolism of Dendritic Cells in Tumor Microenvironment: For Immunotherapy. Front Immunol 12, 613492. 10.3389/fimmu.2021.613492. [PubMed: 33732237]
121. Watson MJ, Vignali PDA, Mullett SJ, Overacre-Delgoffe AE, Peralta RM, Grebinoski S, Menk AV, Rittenhouse NL, DePeaux K, Whetstone RD, et al. (2021). Metabolic support of tumour-infiltrating regulatory T cells by lactic acid. Nature 591, 645–651. 10.1038/s41586-020-03045-2. [PubMed: 33589820]
122. Nussing S, Trapani JA, and Parish IA (2020). Revisiting T Cell Tolerance as a Checkpoint Target for Cancer Immunotherapy. Front Immunol 11, 589641. 10.3389/fimmu.2020.589641. [PubMed: 33072137]
123. Wohn C, Le Guen V, Voluzan O, Fiore F, Henri S, and Malissen B (2020). Absence of MHC class II on cDC1 dendritic cells triggers fatal autoimmunity to a cross-presented self-antigen. Sci Immunol 5. 10.1126/sciimmunol.aba1896.
124. Ruhland MK, Roberts EW, Cai E, Mujal AM, Marchuk K, Beppler C, Nam D, Serwas NK, Binnewies M, and Krummel MF (2020). Visualizing Synaptic Transfer of Tumor Antigens among Dendritic Cells. Cancer Cell 37, 786–799 e785. 10.1016/j.ccell.2020.05.002. [PubMed: 32516589]
125. de Mingo Pulido A, Gardner A, Hiebler S, Soliman H, Rugo HS, Krummel MF, Coussens LM, and Ruffell B (2018). TIM-3 Regulates CD103(+) Dendritic Cell Function and Response to Chemotherapy in Breast Cancer. Cancer Cell 33, 60–74 e66. 10.1016/j.ccell.2017.11.019. [PubMed: 29316433]
126. Gerner MY, Kastenmuller W, Ifrim I, Kabat J, and Germain RN (2012). Histo-cytometry: a method for highly multiplex quantitative tissue imaging analysis applied to dendritic cell subset microanatomy in lymph nodes. Immunity 37, 364–376. 10.1016/j.immuni.2012.07.011. [PubMed: 22863836]
127. Momin N, Mehta NK, Bennett NR, Ma L, Palmeri JR, Chinn MM, Lutz EA, Kang B, Irvine DJ, Spranger S, and Wittrup KD (2019). Anchoring of intratumorally administered cytokines to collagen safely potentiates systemic cancer immunotherapy. Sci Transl Med 11. 10.1126/scitranslmed.aaw2614.

128. Zhu EF, Gai SA, Opel CF, Kwan BH, Surana R, Mihm MC, Kauke MJ, Moynihan KD, Angelini A, Williams RT, et al. (2015). Synergistic innate and adaptive immune response to combination immunotherapy with anti-tumor antigen antibodies and extended serum half-life IL-2. Cancer Cell 27, 489–501. 10.1016/j.ccell.2015.03.004. [PubMed: 25873172]
129. Hughes TK, Wadsworth MH 2nd, Gierahn TM, Do T, Weiss D, Andrade PR, Ma F, de Andrade Silva BJ, Shao S, Tsoi LC, et al. (2020). Second-Strand Synthesis-Based Massively Parallel scRNA-Seq Reveals Cellular States and Molecular Features of Human Inflammatory Skin Pathologies. Immunity 53, 878–894 e877. 10.1016/j.immuni.2020.09.015. [PubMed: 33053333]
130. Gierahn TM, Wadsworth MH 2nd, Hughes TK, Bryson BD, Butler A, Satija R, Fortune S, Love JC, and Shalek AK (2017). Seq-Well: portable, low-cost RNA sequencing of single cells at high throughput. Nat Methods 14, 395–398. 10.1038/nmeth.4179. [PubMed: 28192419]
131. Stoeckius M, Zheng S, Houck-Loomis B, Hao S, Yeung BZ, Mauck WM 3rd, Smibert P, and Satija R (2018). Cell Hashing with barcoded antibodies enables multiplexing and doublet detection for single cell genomics. Genome Biol 19, 224. 10.1186/s13059-018-1603-1. [PubMed: 30567574]
132. Roelli P, Flynn B, and Gui G (2019). Hoohm/CITE-seq-Count: 1.4.2. (Version 1.4.2). Zenodo 10.5281/zenodo.2590196.
133. Macosko EZ, Basu A, Satija R, Nemesh J, Shekhar K, Goldman M, Tirosh I, Bialas AR, Kamitaki N, Martersteck EM, et al. (2015). Highly Parallel Genome-wide Expression Profiling of Individual Cells Using Nanoliter Droplets. Cell 161, 1202–1214. 10.1016/j.cell.2015.05.002. [PubMed: 26000488]
134. Hafemeister C, and Satija R (2019). Normalization and variance stabilization of single-cell RNA-seq data using regularized negative binomial regression. Genome Biol 20, 296. 10.1186/s13059-019-1874-1. [PubMed: 31870423]
135. Butler A, Hoffman P, Smibert P, Papalexi E, and Satija R (2018). Integrating single-cell transcriptomic data across different conditions, technologies, and species. Nat Biotechnol 36, 411–420. 10.1038/nbt.4096. [PubMed: 29608179]
136. Liberzon A, Subramanian A, Pinchback R, Thorvaldsdottir H, Tamayo P, and Mesirov JP (2011). Molecular signatures database (MSigDB) 3.0. Bioinformatics 27, 1739–1740. 10.1093/bioinformatics/btr260. [PubMed: 21546393]
137. Tu AA, Gierahn TM, Monian B, Morgan DM, Mehta NK, Ruiter B, Shreffler WG, Shalek AK, and Love JC (2019). TCR sequencing paired with massively parallel 3' RNA-seq reveals clonotypic T cell signatures. Nat Immunol 20, 1692–1699. 10.1038/s41590-019-0544-5. [PubMed: 31745340]
138. Vander Heiden JA, Yaari G, Uduman M, Stern JN, O'Connor KC, Hafler DA, Vigneault F, and Kleinstein SH (2014). pRESTO: a toolkit for processing high-throughput sequencing raw reads of lymphocyte receptor repertoires. Bioinformatics 30, 1930–1932. 10.1093/bioinformatics/btu138. [PubMed: 24618469]
139. Gupta NT, Vander Heiden JA, Uduman M, Gadala-Maria D, Yaari G, and Kleinstein SH (2015). Change-O: a toolkit for analyzing large-scale B cell immunoglobulin repertoire sequencing data. Bioinformatics 31, 3356–3358. 10.1093/bioinformatics/btv359. [PubMed: 26069265]
140. Smith TS, Heger A, and Sudbery I (2017). UMI-tools: Modelling sequencing errors in Unique Molecular Identifiers to improve quantification accuracy. Genome Research 27, 491–499. 10.1101/gr.209601.116. [PubMed: 28100584]
141. Burger ML, Cruz AM, Crossland GE, Gaglia G, Ritch CC, Blatt SE, Bhutkar A, Canner D, Kienka T, Tavana SZ, et al. (2021). Antigen dominance hierarchies shape TCF1(+) progenitor CD8 T cell phenotypes in tumors. Cell 184, 4996–5014 e4926. 10.1016/j.cell.2021.08.020. [PubMed: 34534464]
142. Liberzon A, Birger C, Thorvaldsdottir H, Ghandi M, Mesirov JP, and Tamayo P (2015). The Molecular Signatures Database (MSigDB) hallmark gene set collection. Cell Syst 1, 417–425. 10.1016/j.cels.2015.12.004. [PubMed: 26771021]
143. Skinner J (2018). Statistics for Immunologists. Curr Protoc Immunol 122, 54. 10.1002/cpim.54. [PubMed: 30400720]

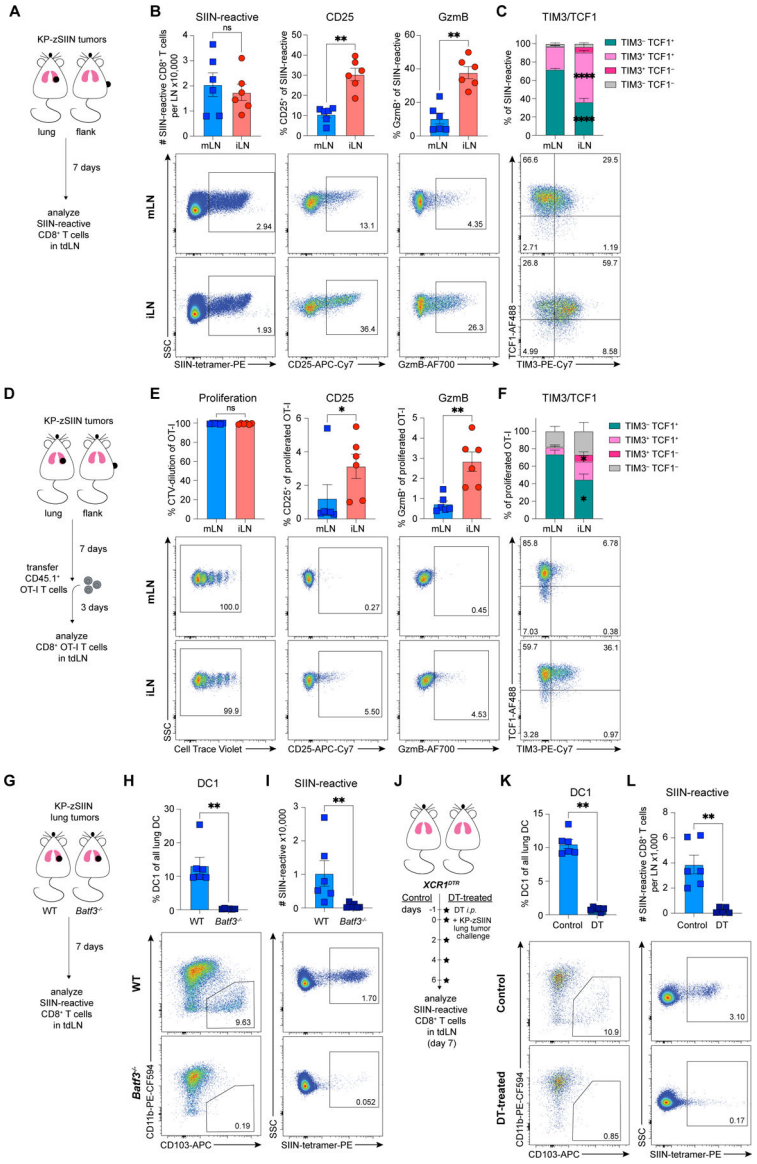

Figure 1. DC1 in mLN prime dysfunctional CD8+ T cells against lung KP tumors.

(A) Experimental design for (B-C).

(B-C) Representative flow plots and (B) numbers or CD25, GzmB, (C) TCF1 and TIM-3 expression of SIIN-reactive CD8$^+$ T cells in tdLN, day 7 post-tumor implantation (n=3 mice/group; two independent experiments).

(D) Experimental design for (E-F).

(E-F) Representative flow plots and quantified (E) CellTrace Violet (CTV)-dilution or CD25, GzmB, (F) TCF1 and TIM-3 expression of adoptively-transferred CTV-labelled OT-I T cells primed in tdLN, day 10 post-tumor implantation (n=3 mice/group; two independent experiments).

(G) Experimental design for (H-I).

(H-I) Representative flow plots and quantified abundance of (H) DC1 in lungs and (I) SIIN-reactive $CD8^+$ T cells in mLN of tumor-bearing WT or *Batf3*$^{-/-}$ mice, day 7 post-tumor implantation (n=3 mice/group; two independent experiments).
(J) Experimental design for (K-L).
(K-L) Representative flow plots and quantified abundance of (K) DC1 in lungs and (L) SIIN-reactive $CD8^+$ T cells in mLN of control or DT-treated tumor-bearing *XCR1*^{DTR} mice, day 7 post-tumor implantation (n=3 mice/group; two independent experiments).
*p<0.05, **p<0.01, ****p<0.0001, ns=not significant; MWU (B-C,E-F,H-I,K-L). Data shown as mean ± SEM.

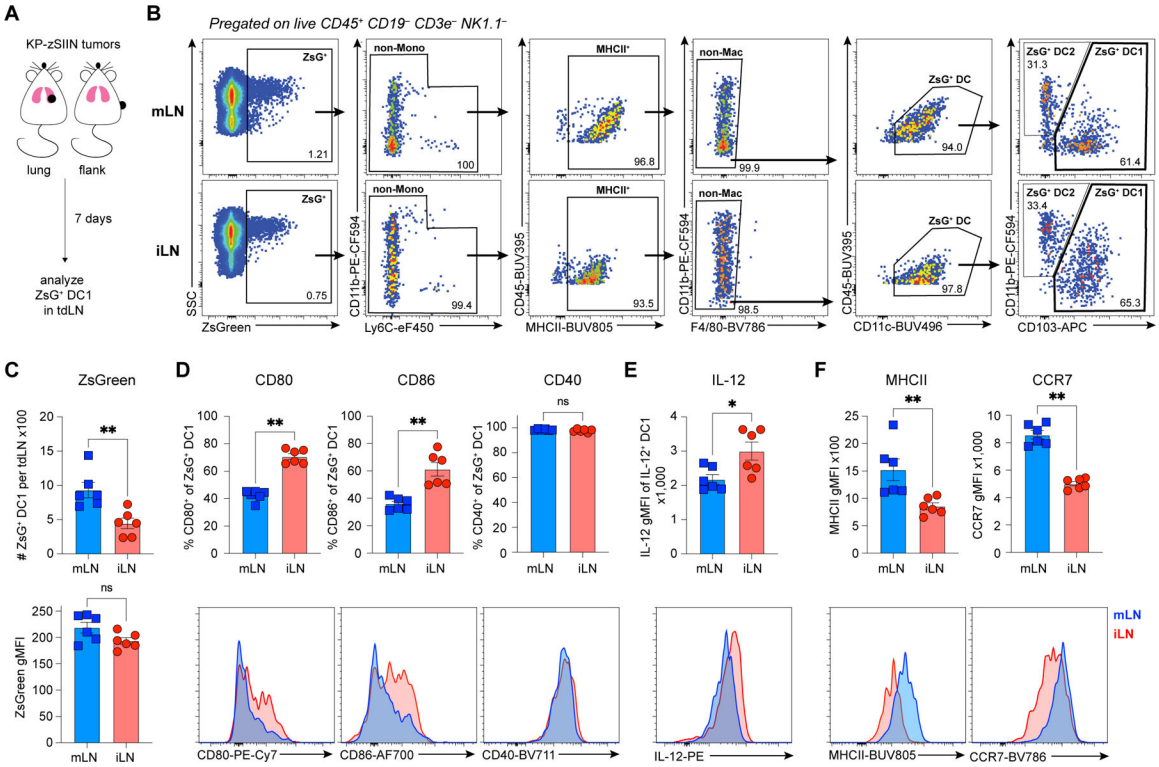

Figure 2. DC1 in tumor-draining mLN have high signal 1, but low signals 2 and 3.

(A) Experimental design for (B-F).

(B) Representative flow gating strategy for ZsG^+ DC1 from tdLN.

(C) (*top*) Abundance and (*bottom*) ZsG geometric mean fluorescence intensity (gMFI) of ZsG^+ DC1 from tdLN, day 7 post-tumor implantation (LN from 3–4 mice pooled per datapoint; two independent experiments).

(D-F) Representative histograms and quantified expression of (D) CD80, CD86, CD40, (E) IL-12, (F) MHCII and CCR7 on ZsG^+ DC1 from tdLN, day 7 post-tumor implantation (LN from 3–4 mice pooled per datapoint; two independent experiments).

*p<0.05, **p<0.01, ns=not significant; MWU (C-F). Data shown as mean ± SEM.

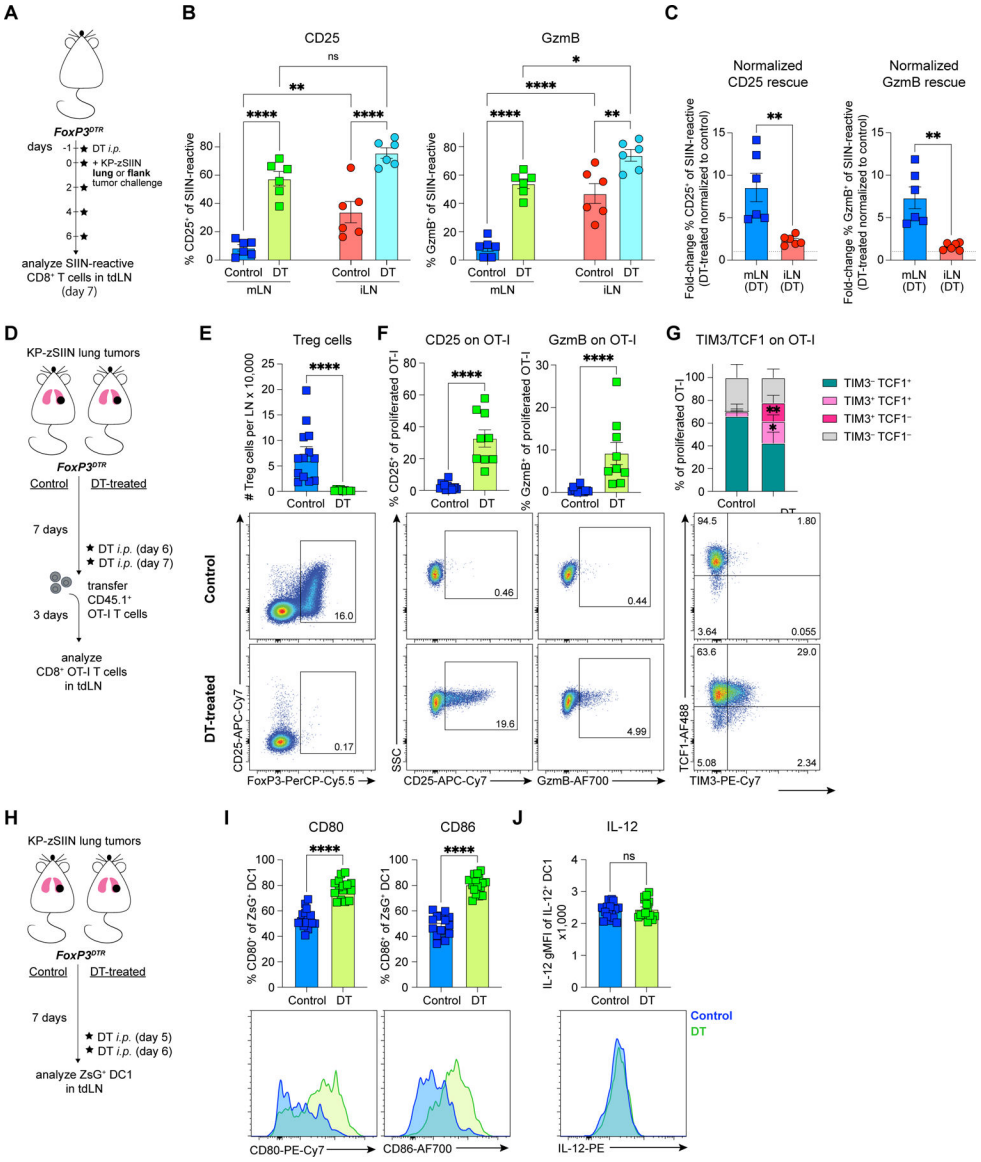

Figure 3. Treg cells can induce CD8+ T cell dysfunction and DC1 suppression in the tumor-draining mLN.

(A) Experimental design for (B-C).

(B-C) Quantification of (B) CD25 and GzmB expression, and (C) DT-treated/control ratios of CD25 and GzmB expression within each tdLN site for SIIN-reactive $CD8^+$ T cells from control or DT-treated tumor-bearing *FoxP3*^{DTR} mice, day 7 post-tumor implantation (n=3 mice/group; two independent experiments).

(D) Experimental design for (E-G).

(E-G) Representative flow plots and quantified (E) Treg cell number, (F) expression of CD25, GzmB, (G) TCF1 and TIM-3 on adoptively-transferred proliferated OT-I T cells from mLN of control or DT-treated tumor-bearing *FoxP3*^{DTR} mice, day 10 post-tumor implantation (n=2–4 mice/group; four independent experiments).

(H) Experimental design for (I-J).

(I-J) Representative histograms and quantified expression of (I) CD80, CD86 and (J) IL-12 on ZsG^{+} DC1 from mLN of control or DT-treated tumor-bearing *FoxP3*^{DTR} mice, day 7 post-tumor implantation (mLN from 3–5 mice pooled per datapoint; six independent experiments).

*p<0.05, **p<0.01, ****p<0.0001, ns=not significant; two-way ANOVA (B), MWU (C,E-G,I-J). Data shown as mean ± SEM.

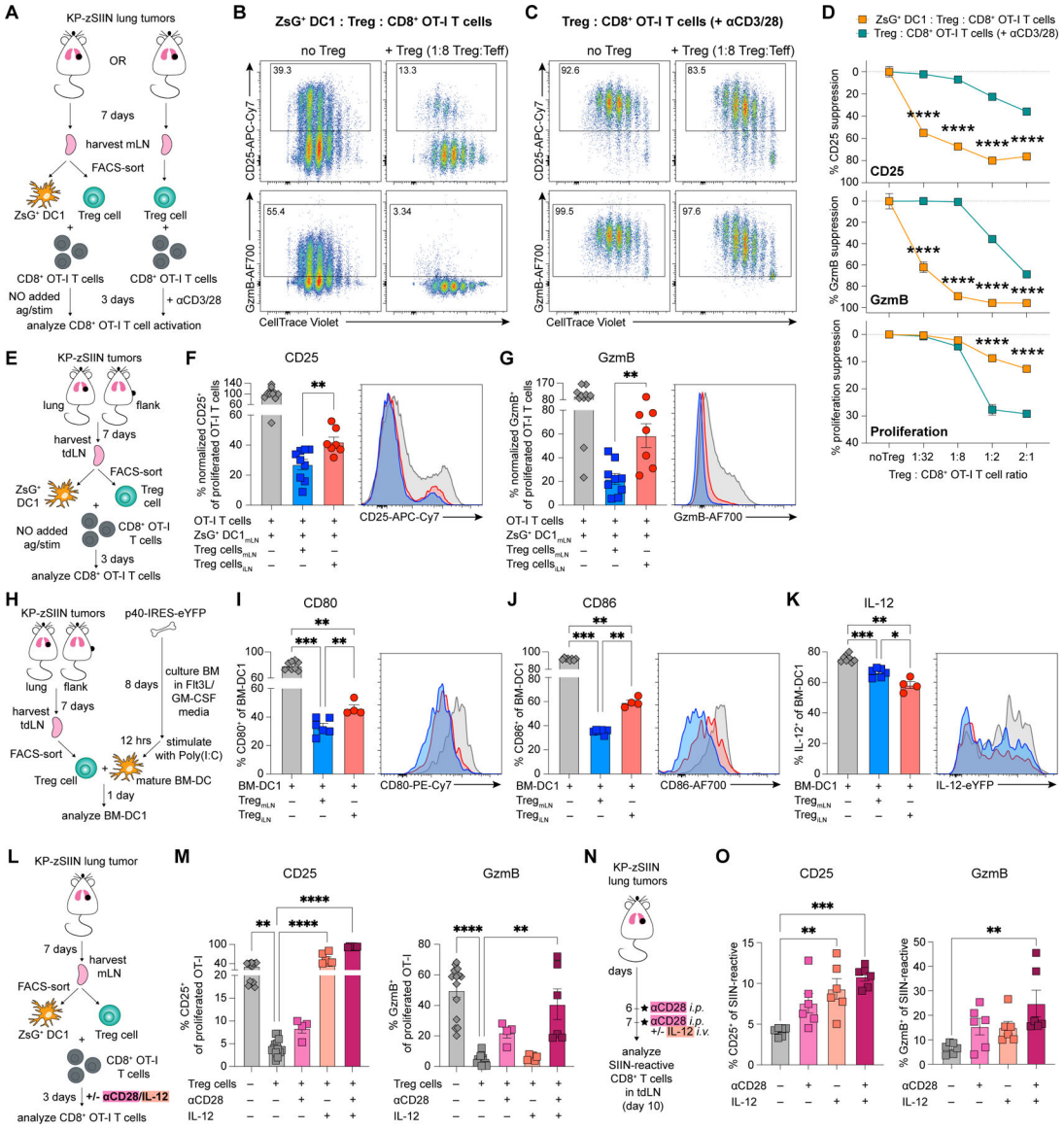

Figure 4. Treg cells from the tumor-draining mLN restrain cytotoxic T cell priming by suppressing DC-derived signals 2 and 3.

(A) Experimental design for (B-D).

(B-D) Representative flow plots of proliferation, CD25 and GzmB expression of CTV-labelled OT-I T cells after 3-day co-culture with (B) mLN-sorted ZsG$^+$ DC1 and Treg cells or (C) mLN-sorted Treg cells with αCD3/αCD28-stimulation; representative example quantified in (D) (50 tdLN pooled for sorting, three independent experiments).

(E) Experimental design for (F-G).

(F-G) Representative histograms and quantified expression of (F) CD25 and (G) GzmB on proliferated OT-I T cells after 3-day co-culture with mLN-sorted ZsG$^+$ DC1 and either mLN- or iLN-sorted Treg cells (50 tdLN pooled for sorting, three independent experiments).

(H) Experimental design for (I-K).

(I-K) Representative histograms and quantified expression of (I) CD80, (J) CD86 and (K) IL-12 on *p40-IRES-eYFP* BM-DC1 after 3-day co-culture with either mLN- or iLN-sorted Treg cells (15 tdLN pooled for sorting, two independent experiments).

(L) Experimental design for (M).

(M) CD25 and GzmB expression on proliferated OT-I T cells after 3-day co-culture with mLN-sorted DC1 and Treg cells at indicated culture conditions (50 mLN pooled for sorting, four independent experiments).

(N) Experimental design for (O).

(O) CD25 and GzmB expression on SIIN-reactive $CD8^+$ T cells in tumor-draining mLN, day 10 post-tumor implantation (n=3 mice/group; two independent experiments).

*p<0.05, **p<0.01, ***p<0.001, ****p<0.0001; two-way ANOVA (D), MWU (F-G,I-K) or KW (M,O). Data shown as mean ± SEM.

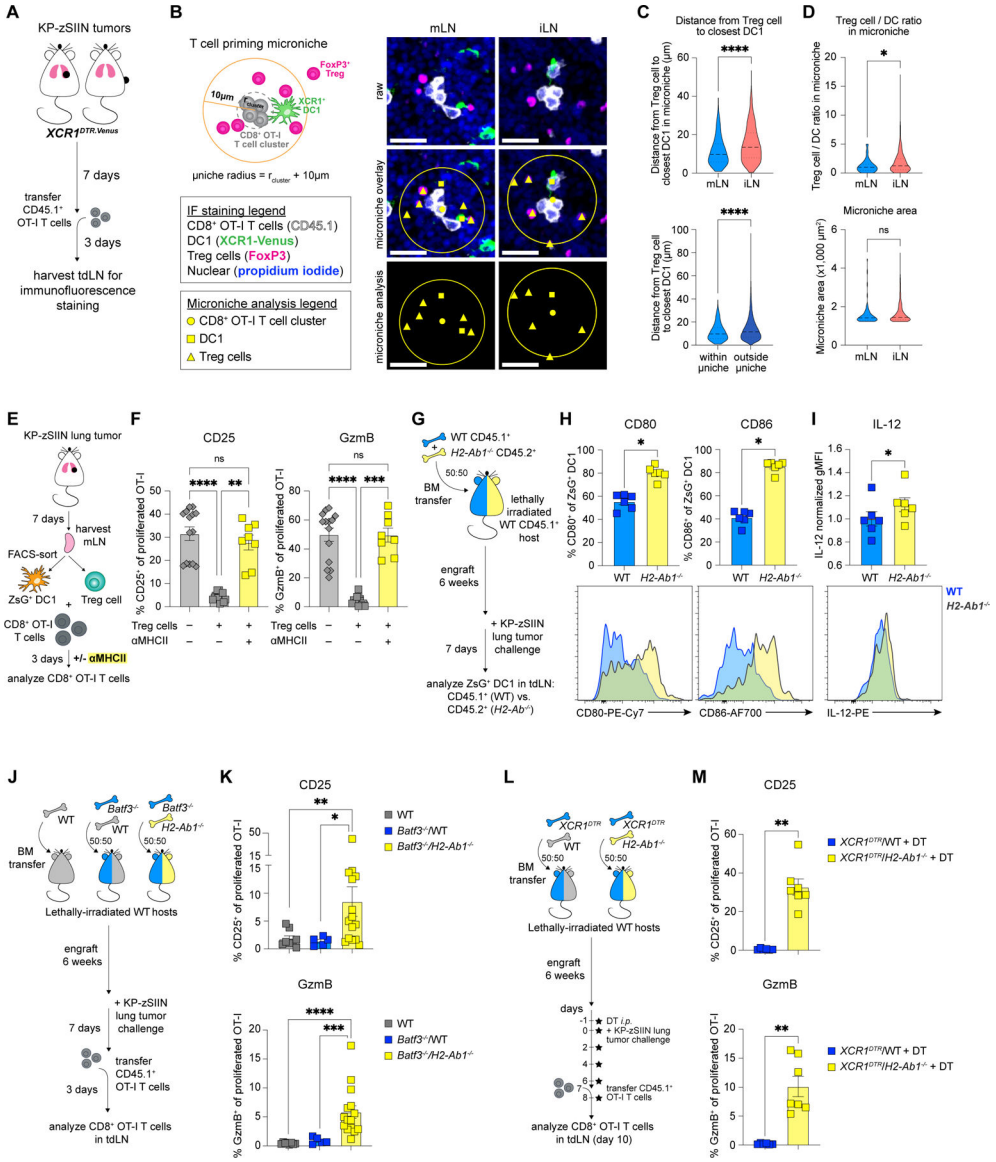

Figure 5. Treg cells suppress CD8+ T cell priming in the mLN via direct interaction with DC1.

(A) Experimental design for (B-D) and Figure S2K.

(B) Schematic of microniche analysis for (C-D) and representative IF images of tdLN from tumor-bearing *XCR1*$^{DTR.Venus}$ mice, day 10 post-tumor implantation; scale bar, 20 μm.

(C-D) Distance from Treg cell to closest DC1 (C, *top*) within microniche in tumor-draining mLN and iLN or (C, *bottom*) in mLN within and outside of microniche, (D, *top*) Treg/DC1 ratio within microniche and (D, *bottom*) microniche area in tdLN; using microniche radius: $r_{cluster}$ + 10μm (n=4 mice/group including 399 mLN microniches and 74 iLN microniches; representative data from one of two independent experiments).

(E) Experimental design for (F).

(F) CD25 and GzmB expression on proliferated OT-I T cells after 3-day co-culture with mLN-sorted ZsG^{+} DC1 and Treg cells at indicated culture conditions (50 mLN pooled for

sorting, four independent experiments); controls (gray bars) are the same as shown in Figure 4M.

(G) Experimental design for (H-I) and Figures S2L-M.

(H-I) Representative histograms and quantified expression of (H) CD80, CD86 and (I) IL-12 on WT and *H2-Ab1*$^{-/-}$ ZsG^{+} DC1 from mLN of tumor-bearing WT/*H2-Ab1*$^{-/-}$ BMCs, day 7 post-tumor implantation (mLN from 3–4 mice pooled per datapoint; two independent experiments).

(J) Experimental design for (K) and Figures S2N-O.

(K) CD25 and GzmB expression on adoptively-transferred proliferated OT-I T cells primed in mLN of tumor-bearing WT, *Batf3*$^{-/-}$/WT or *Batf3*$^{-/-}$/*H2-Ab1*$^{-/-}$ BMCs, day 10 post-tumor implantation (n=2–5 mice/group; 1–4 independent experiments).

(L) Experimental design for (M) and Figures S2P-Q.

(M) CD25 and GzmB expression on adoptively-transferred proliferated OT-I T cells primed in mLN of DT-treated tumor-bearing *XCR1*^{DTR}/WT or *XCR1*^{DTR}/*H2-Ab1*$^{-/-}$ BMCs, day 10 post-tumor implantation (n=3–4 mice/group; two independent experiments).

*p<0.05, **p<0.01, ***p<0.001, ****p<0.0001, ns=not significant; MWU test (C-D,K,M), paired-MWU (H-I) or KW (F). Data shown as mean ± SEM.

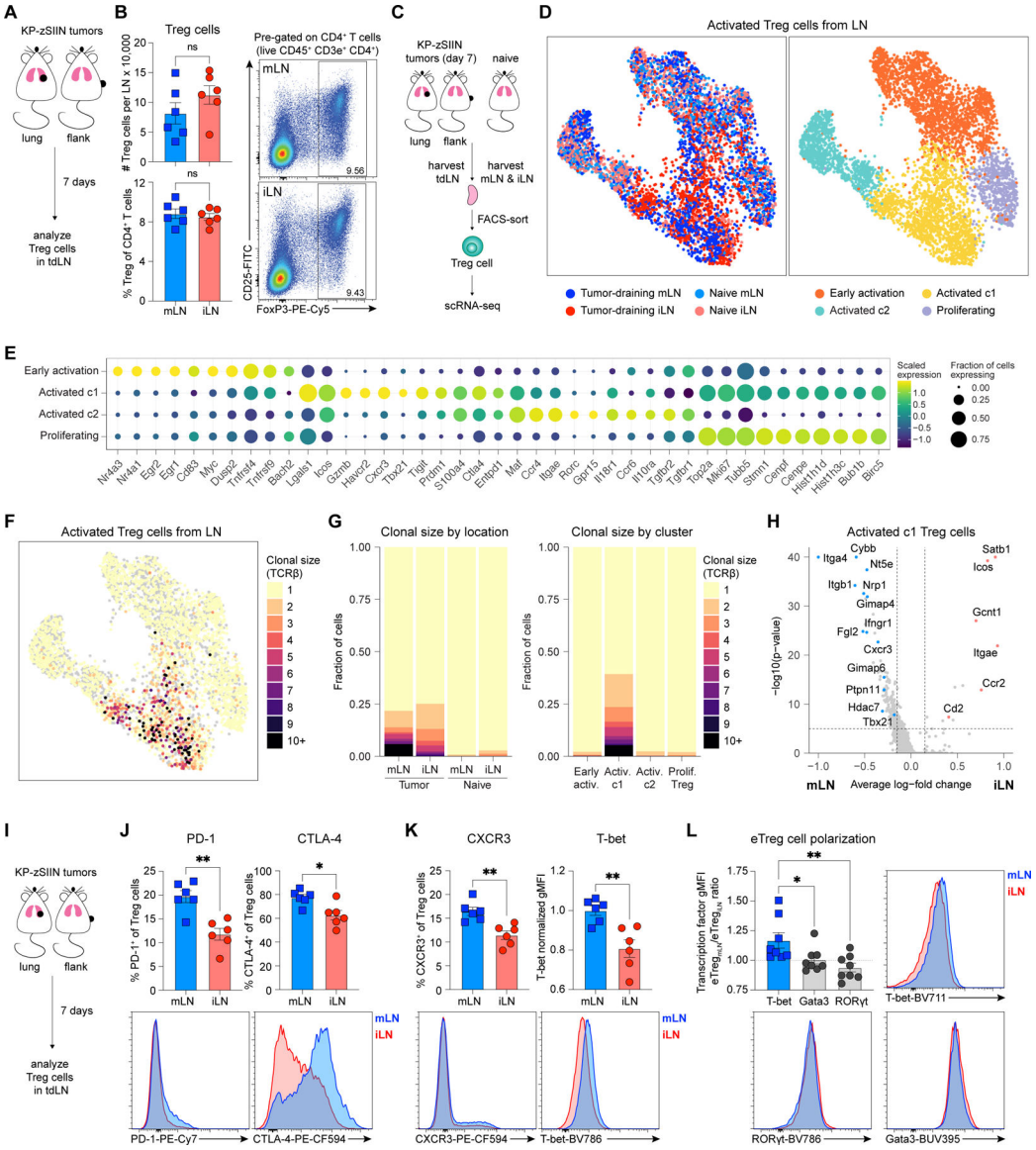

Figure 6. TH1-like Treg cells expand in tumor-draining mLN.

(A) Experimental design for (B) and Figure S3A.

(B) Representative flow plots and quantified abundance of Treg cells in tdLN, day 7 post-tumor implantation (n=3 mice/group; two independent experiments).

(C) Experimental design for (D-H) and Figures S3B-K;S3N.

(D) UMAP plots of activated Treg cells from naïve and tumor-draining mLN and iLN colored (*left*) by tumor status and location or (*right*) by cluster (tdLN, n=5 mice/group; naïve LN, n=20 mice/group).

(E) Dot plot of select marker genes for each Treg cluster displaying average expression and frequency of expression for each gene.

(F-G) Clonal size of activated Treg cells (F) mapped onto UMAP plot and (G) graphed using stacked bar plots arranged (*left*) by tumor status and location or (*right*) by cluster.

(H) Volcano plot of DEGs between activated c1 Treg cells from mLN and iLN.

(I) Experimental design for (J-L).
(J-K) Representative histograms and quantified expression of (J) PD-1, CTLA-4, (K) CXCR3 and T-bet on Treg cells from tdLN, day 7 post-tumor implantation (n=3 mice/group; two independent experiments).
(L) Representative histograms and transcription factor gMFI ratios for eTreg cells from tumor-draining mLN and iLN, day 7 post-tumor implantation (n=4 mice/group; two independent experiments).
*p<0.05, **p<0.01, ns=not significant; MWU (B,J-L), MWU with Bonferroni correction (H). Data shown as mean ± SEM.

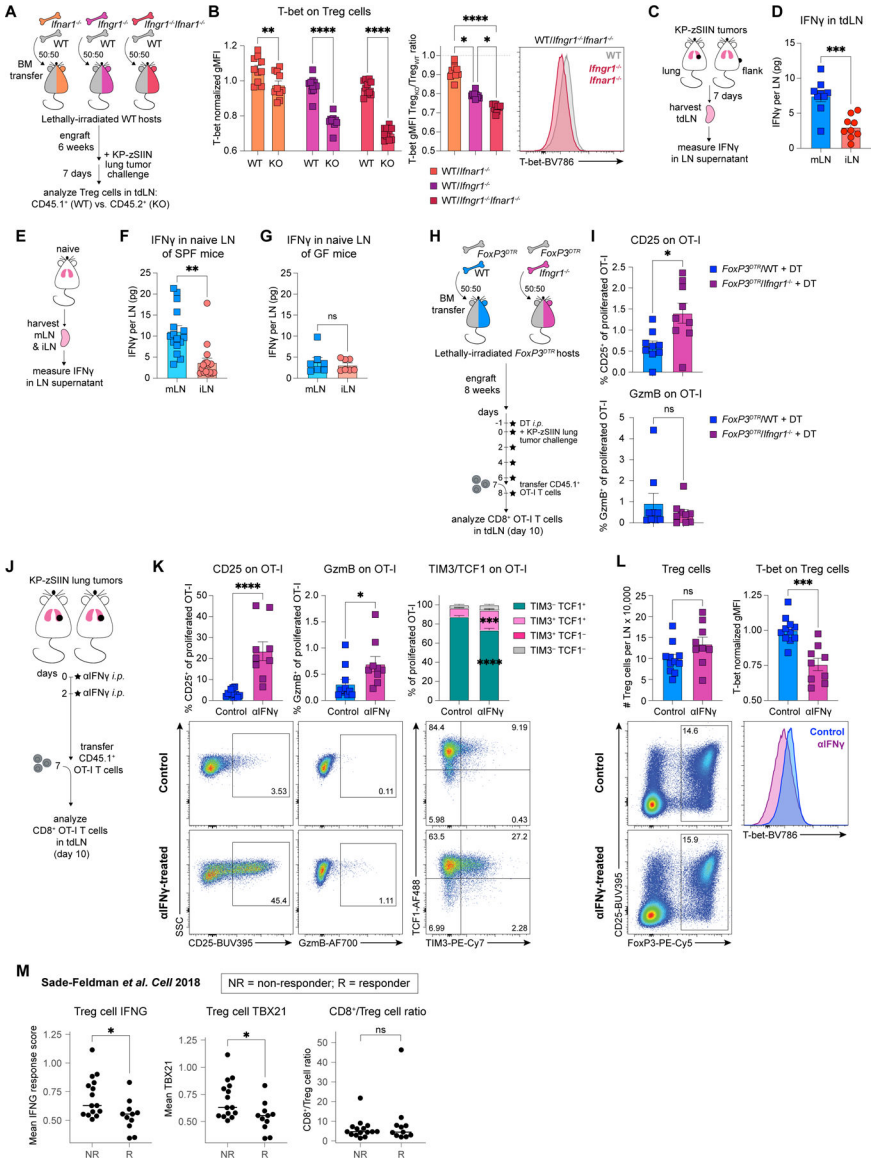

Figure 7. mLN-specific enrichment in IFNγ drives induction of TH1-like Treg cells and the associated dysfunctional T cell responses against lung cancer.

(A) Experimental design for (B).

(B) Representative histogram and quantified T-bet expression on WT and IFN receptor-deficient (KO) Treg cells from mLN of tumor-bearing WT/*Ifnar1*$^{-/-}$, WT/*Ifngr1*$^{-/-}$ or WT/*Ifngr1*$^{-/-}$*Ifnar1*$^{-/-}$ BMCs, day 7 post-tumor implantation (n=5 mice/group; two independent experiments).

(C) Experimental design for (D).

(D) IFNγ quantification in tdLN, day 7 post-tumor implantation (n=3 mice/group; three independent experiments).

(E) Experimental design for (F-G).

(F) IFNγ quantification in LN of naïve SPF mice (n=3–4 mice/group; five independent experiments).

(G) IFNγ quantification in LN of naïve GF mice (n=2–3 mice/group; three independent experiments).
(H) Experimental design for (I).
(I) CD25 and GzmB expression on adoptively-transferred proliferated OT-I T cells primed in mLN of DT-treated tumor-bearing *FoxP3*^{DTR}/WT or *FoxP3*^{DTR}/*Ifngr1*$^{-/-}$ BMCs, day 10 post-tumor implantation (n=3 mice/group; three independent experiments).
(J) Experimental design for (K-L).
(K-L) Representative flow plots and quantified expression of (K) CD25, GzmB, TIM3 and TCF1 on adoptively-transferred proliferated OT-I T cells and (L) abundance and T-bet expression for Treg cells from mLN of control and αIFNγ-treated tumor-bearing mice, day 10 post-tumor implantation (n=3–4 mice/group; three independent experiments).
(M) IFNG response hallmark signature scores and *TBX21* expression on intratumoral Treg cells, along with CD8^{+}/Treg cell ratios in melanoma patients, including ICB-responders (R) and ICB-non-responders (NR)[103].
*p<0.05, **p<0.01, ***p<0.001, ****p<0.0001, ns=not significant; two-way ANOVA (B, *left*) or KW (B, *middle*), paired-MWU (F-G), MWU (D,I,K-L,M). Data shown as mean ± SEM, except in (M) where the median is shown.